Investigation of 1064-nm laser fluence within tissue phantoms and its in vivo effects on human brain networks

by

Hasan Parvez

1001290688

Presented to the Faculty of the Graduate School of

The University of Texas at Arlington in Partial Fulfillment

of the Requirements

for the Degree of

MASTER OF SCIENCE IN BIOMEDICAL ENGINEERING

THE UNIVERSITY OF TEXAS AT ARLINGTON

May 2018

ACKNOWLEDGEMENTS

I would like to express my gratitude to Prof. Dr. Hanli Liu for her support, motivation and persistent guidance in my master's research project. Her immense knowledge, effective approach towards work, and guidance helped me in all the time of research and writing of this thesis. I wish to thank my committee members Dr. George Alexandrakis and Dr. Yuan B Peng for their time, and valuable suggestions to improve this manuscript.

I am grateful to Dr . Xinlong Wang for helping me in data collection, data processing and analysis of the results. Besides, I would like to express my special thanks to my lab mates: Mr. Sahil Nalawade, Ms. Divya Reddy, Ms. Madhumita Srikanth, Mr. Tyrell Puritt, and Mr. Yudhajit Das.

Finally, special thanks to my parents Mr. Atique Parvez Bhatti and Ms. Abida Sultana, my siblings: Dr. Mehwish Parvez and Ms. Zara Parvez, and my wife: Ms. Shazia Hasan Khan, for their moral support and unconditional love.

May 08, 2018

ABSTRACT

INVESTIGATION OF 1064-NM LASER FLUENCE WITHIN TISSUE PHANTOMS AND ITS IN VIVO EFFECTS ON HUMAN BRAIN NETWORKS

Hasan Parvez, M.S.

The University of Texas at Arlington, 2018

Supervising Professor: Dr. Hanli Liu

For the past few decades there has been an increasing interest in the usage of near infrared (NIR) laser in the medical optics field. This is due to a number of studies conducted on different animal models utilizing NIR laser, which was reported to provide improvement in such cognitive functions as memory, decision making, and executive functions. The NIR laser produces no adverse effects in the human tissue, having a potential for treating different neurological disorders. However, there is limited knowledge related to the underlying mechanism of photon interaction with the human tissue. In this thesis, I tried to address this issue by conducting two separate studies.

For the first study, a series of different experimental protocols were performed utilizing laboratory tissue phantoms along with the 1064-nm laser. The goal of this part was to determine the dependence of optical fluence within the tissue phantom on (a) the power, (b) the beam size, and (c) the penetration depth of the laser. The results of the phantom study showed that optical fluence (1) had a linear relationship with the power of 1064-nm laser, (2) decreased with an increase in penetration depth. Also, an analytical expression was derived and proved to match well with the experimental results.

For the second part of study, I was interested in observing the modulation of electrophysiological signals in the human by the administration of 1064-nm laser. The experimental protocol included two different treatment groups, namely, the placebo treatment group and laser treatment group. In both treatment groups, right forehead of each subject was stimulated with different laser doses of the 1064-nm laser source. Electrophysiological data was recorded through the 64-channel EEG from 20 human subjects, and the functional connectivity was estimated using Pearson correlation coefficient (r). Statistically significant changes across different regions of the brain network were determined by comparing the two treatment groups. The results reported significant changes by the 1064-nm laser in the low-frequency oscillation bands, namely, the theta (4-7 Hz) and alpha (8-13 Hz) band. Both bands showed significantly enhanced connectivity in the frontal and occipito-parietal region. The total number of significant connections were increased during the treatment of laser. This study provided the first demonstration that transcranial infrared laser stimulation caused the modulation of lower-frequency oscillation bands in the human brain.

Table of Contents

LIST OF ILLUSTRATIONS

CHAPTER 1

INTRODUCTION

1.1 Introduction to optical imaging

Optical imaging is utilized to study different characteristics of human tissue, non-invasively without any exposure to harmful radiations. It has many applications ranging from the functional study of the human brain to detecting the different types of cancer, as it provides functional information of different tissue types [1, 2]. In tissue optics, the wavelength of a light source is significant as photons are absorbed and scattered by tissue differently in each wavelength range [3].

A particular optical window is generally selected where light absorption is minimal by different tissue chromophores [3]. It is often in the electromagnetic spectrum where light is almost transparent to the tissue or less absorbed. When light interacts with human tissue, it depends on the intrinsic property of light scattering and absorption of photons [4]. Such optical characteristics of human tissue can be used to determine various clinical conditions, as well as to differentiate healthy tissue from diseased tissue [2].

1.2 Introduction to Transcranial Photo Bio-Modulation

The light in the red to the infrared region from 700nm to 1100nm penetrates deep into most of tissue types [5]. Photo-Biomodulation(PBM) has been used a light therapy for healing wounds, relieving pain, rejuvenating human skin, and treating different types of injuries [6-9].

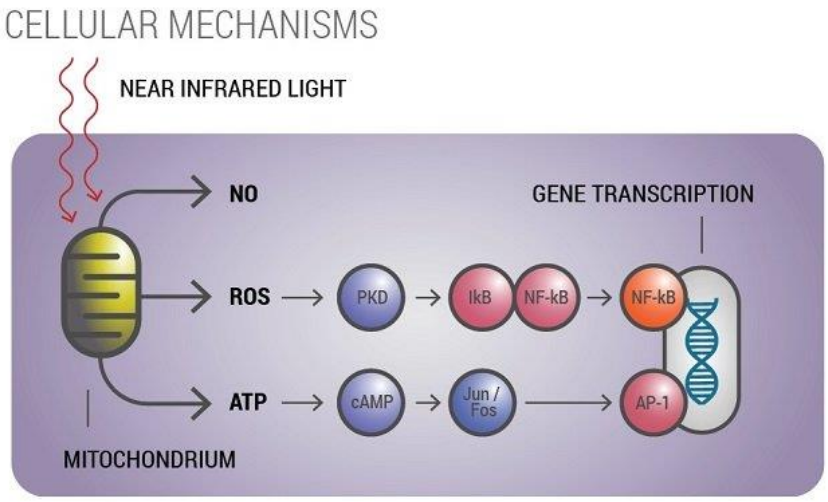

Figure 1.1: Cellular mechanism of Photo-biomodulation
[Reference: https://vielight.com/photobiomodulation/]

The cellular mechanism of photo-biomodulation is illustrated in figure 1.1. A neuron is the major cell type within the brain, and all neurons contain mitochondria. When a cell is irradiated by the red to near-infrared light, many of the photons are absorbed by mitochondria and converted into energy and produces ATP. This process leads to the formation of reactive oxygen species (ROS), which helps in cell healing and repair. In addition, the absorption of photons also leads to release of nitric oxide from the cell, which is a vasodilator and helps in regulating the blood circulation [10].

The effects of PBM were first observed on the animal model by Endre Mester in 1968. He used a laser with a fraction of the power of the ruby laser. He was unable to cure cancer, but it promoted the growth of hair in an animal model at the site of the tumor [11].

For the past several years, there has been an increasing interest in the application of photobiomodulation by near infrared (NIR) or infrared laser or light emitting diodes (LEDs),

which are being successfully implemented for the treatment of different kinds of pain and injuries [4, 12]. Photo biomodulation through low level laser stimulation reduces harmful effects of toxins, increases longevity of neurons, and prevents neuron damage by playing a crucial role in neuroprotection [13].

Neuro-degenerative diseases primarily affect the neurons of the human brain. Photo biomodulation has also shown promising results in cell proliferation. In one of the studies, it was observed that mesenchymal stem cells (MSCs) and cardiac stem cells (CSCs) exhibited increased proliferation of cells when being irradiated by PBM in vitro [14]. In addition, PBM is beneficial in the enhancement of liver regeneration after hepatectomy and liver angiogenesis during liver regeneration [15]. The growth of cells is significantly increased by PBM and it can be used in improving neurogenesis [16].

Multiple in vivo studies are carried out in animal models to investigate effects of Transcranial photo-biomodulation. One study reported the improvement of memory function and visual discrimination in rats by transcranial photobiomodulation (TPBM) [17, 18]. Learning, spatial memory, and cognitive perception were improved by the application of TPBM in mice which had Traumatic Brain Injury (TBI) [19].

Many neurological disorders are due to the imbalance of neurotransmitter and dysfunction of mitochondria. TPBM increases the energy of mitochondria and it is examined to treat many psychological disorders [20]. The single session of TPBM can cause the increase of regional cerebral blood flow [21]. Stroke patients, who had less than 50% lesions in the motor pathway, showed improvement with the use of photo-biomodulation [22]. Moreover, one

study on Alzheimer's disease reported that there was an improvement of cerebral microcirculation, a decrease in dementia, and reduction of cognitive impairment by utilizing TPBM [23].

TPBM protects neurons from cell death and promotes neurogenesis [24]. The human brain can heal itself by the administration of TPBM [19]. It may have a potential in the near future for the treatment of certain neurological disorders, such as depression, psychiatric disorders, Alzheimer's disease, Parkinson's disease, and traumatic brain injury [13, 25]. This implies that TPBM has a wide range of applications in neuroscience than previously thought.

1.3 The human brain and EEG

The Human brain is a major part of the central nervous system and plays a significant role in coordinating different systems of the human body. It is divided into four different lobes: the frontal lobe, temporal lobe, parietal lobe, and occipital lobe.

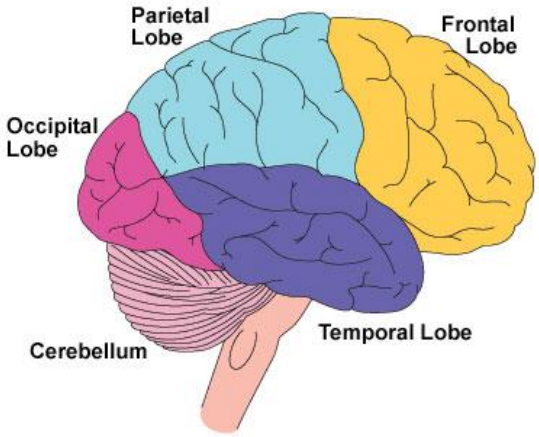

Figure 1.2: Different lobes of the human brain
[Reference: https://blog.cognifit.com/frontal-lobe/]

The different lobes of the brain are illustrated in figure 1.2. Each lobe of the human brain is responsible for the execution of specific tasks. The frontal lobe of the brain is responsible for cognitive and higher executive functions, which are involved in planning and problem-solving. The temporal lobe is responsible for the processing of auditory information, which includes the language recognition. It is also responsible for the higher visual processing. The parietal lobe is involved in the processing of sensory information and helps us to navigate and locate our body in space. The occipital lobe is located at the posterior side of the human brain; it is responsible for processing and interpreting the visual information.

A neuron is the fundamental unit of the central nervous system and the human brain is composed of 100 billion neurons. On the basis of neuron anatomy, there are classified into three different types: unipolar, bipolar and multipolar.

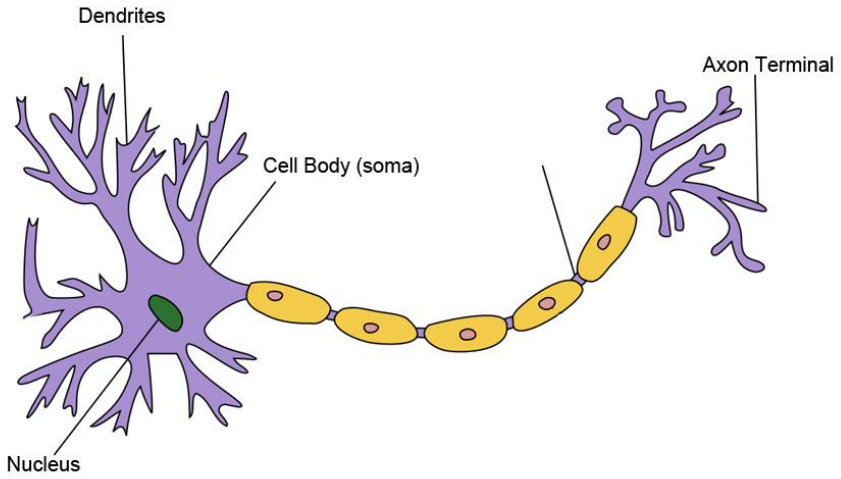

Figure 1.3: Structure of a neuron
[Reference: https://en.wikipedia.org/wiki/Neuron]

Structure of a typical neuron is illustrated in figure 1.3. A neuron is composed of different parts: dendrites, cell body or soma, nucleus, and an axon. The connection of one neuron to another is called synapse. Synapse can be between postsynaptic dendrites or soma of a neuron and a pre-synaptic neuron axon. Depending on the type of task response, neurons can communicate either in the form of electrical signals or chemical signals at synapses. Since a neuron can be excited by electrical activity, we can utilize this property of the brain to record and study the brain activity.

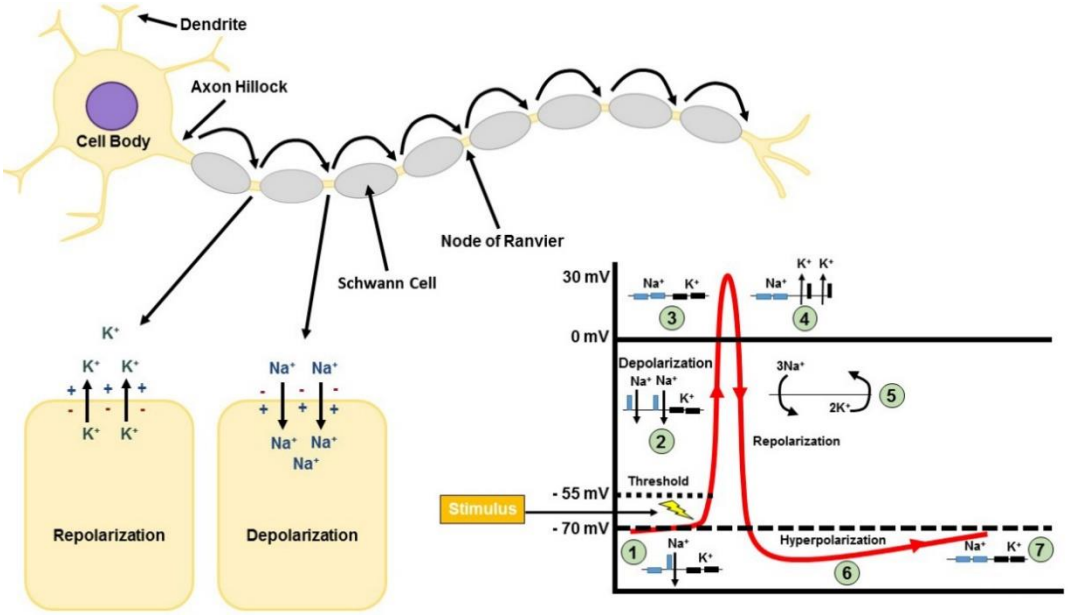

Figure 1.4: Propagation of action potential across the neuron
[Reference: http://step1.medbullets.com/neurology/113052/action-potential-basics]

The propagation of action potential across a neuron is illustrated in figure 1.4. The resting potential of a neuron is -70mv; as soon as it receives a stimulus it depolarizes. This is due to sodium ions influx that makes the membrane potential positive. At +40 mv, sodium

channels close; in the meantime, there is an opening of potassium channels, which cause the efflux of potassium ions. As a result, there is a repolarization of the membrane towards the resting potential. However, cell membranes hyperpolarize to -90 mv before it reaches the resting cell membrane potential of -70 mv.

EEG stands for Electroencephalography. Electrical activity of the human brain can be recorded non invasively and without any exposure to radiations using EEG. It involves the use of electrodes which are sensitive in detecting weak electrical signals in the milli-volts range from the human scalp. An EEG system has different standards of electrode mortgages, such as 10/20 system, 10/10 system, and 10/5 system. The 10/20 system has only 21 electrodes, 10/10 system has 81 electrodes, and 10/5 system has 128 electrodes or more, for recording data precisely from different locations on the human scalp [26]. Moreover, EEG has a high temporal resolution; its signals can be analyzed in different frequency bands [27].

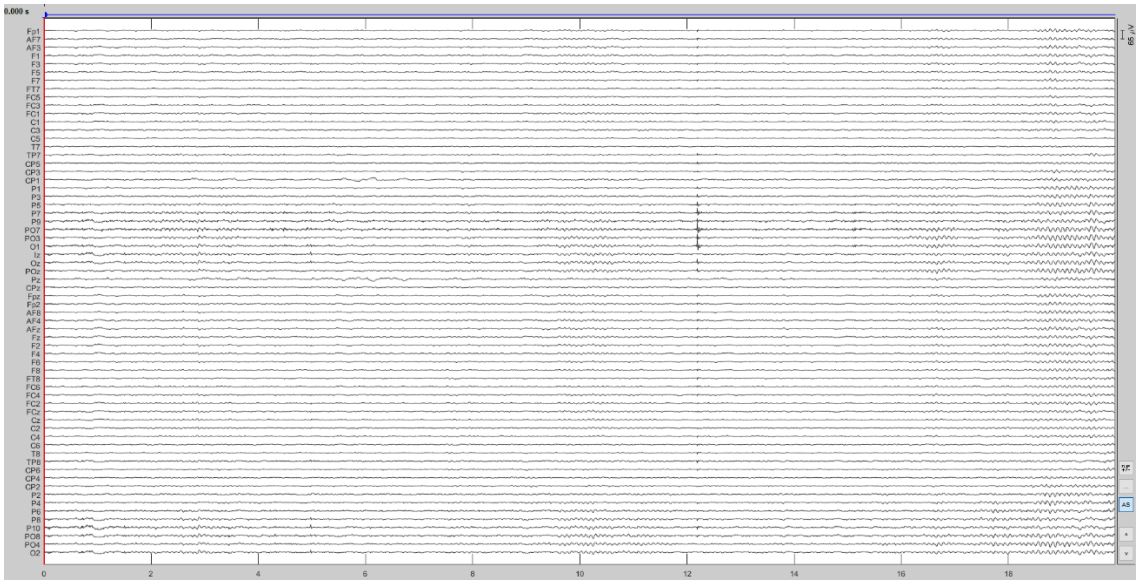

Figure 1.5: An example of acquired EEG Data by a 64-channel EEG system. The x-axis represents time in seconds and Y-axis represents voltage in millivolts.

Data acquired through a 64-channel EEG system is illustrated in figure 1.5. In general, EEG signals are prone to many different noises, such as mainline noise from the electric supply, muscle movement, heartbeat, and etc. We need to remove these noises from raw EEG data. Power spectral density (PSD) is the distribution of power into frequency components [28]. Comparison of PSD before and after the application of a notch filter on EEG data is illustrated in figure 1.6. It is shown in figure 1.6(a) that EEG signal is prone to the mainline frequency at 60 Hz and its harmonic 120 Hz. After the application of the notch filter at 60 Hz and 120 Hz, the mainline frequencies are removed as depicted in 1.6(b).

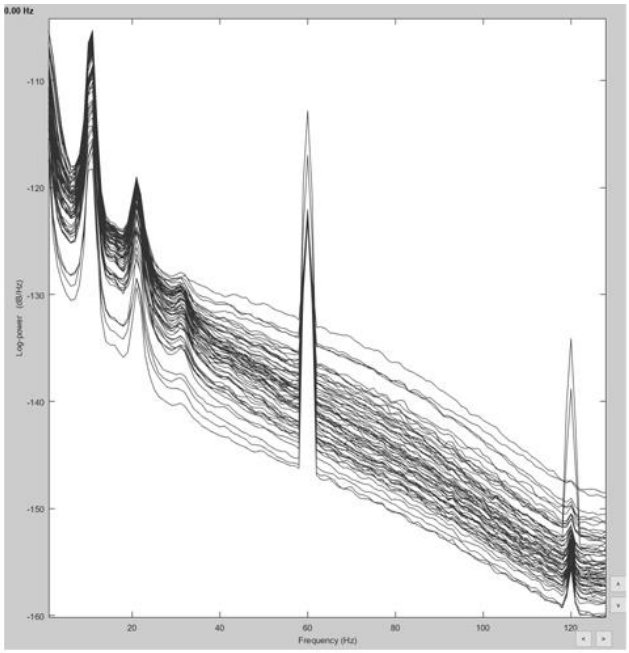

1.6 (a)

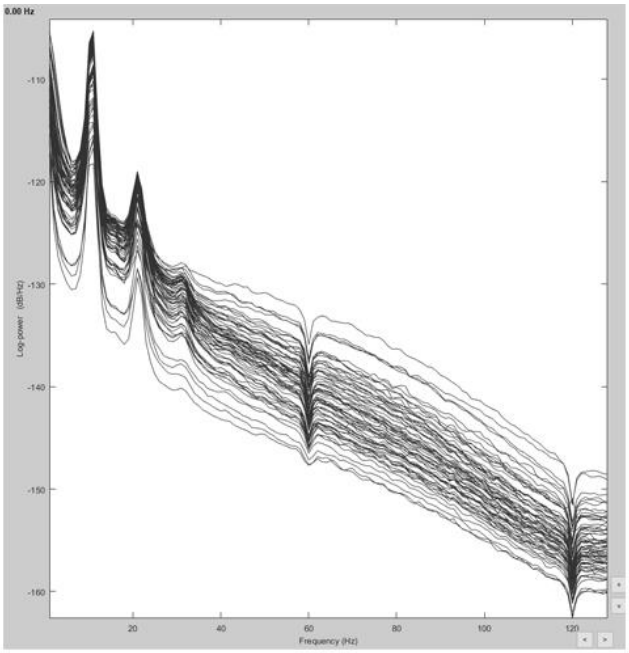

1.6 (b)

Figure 1.6: Power spectral density (PSD) of EEG data. PSD, before a notch filter is applied on the EEG data, is illustrated in figure 1.5 (a). Moreover, PSD after the notch filter is applied at 60 Hz and 120 Hz on EEG data is illustrated in figure 1.5 (b). The x-axis represents frequency in Hz and Y-axis represents log-power in dB/Hz.

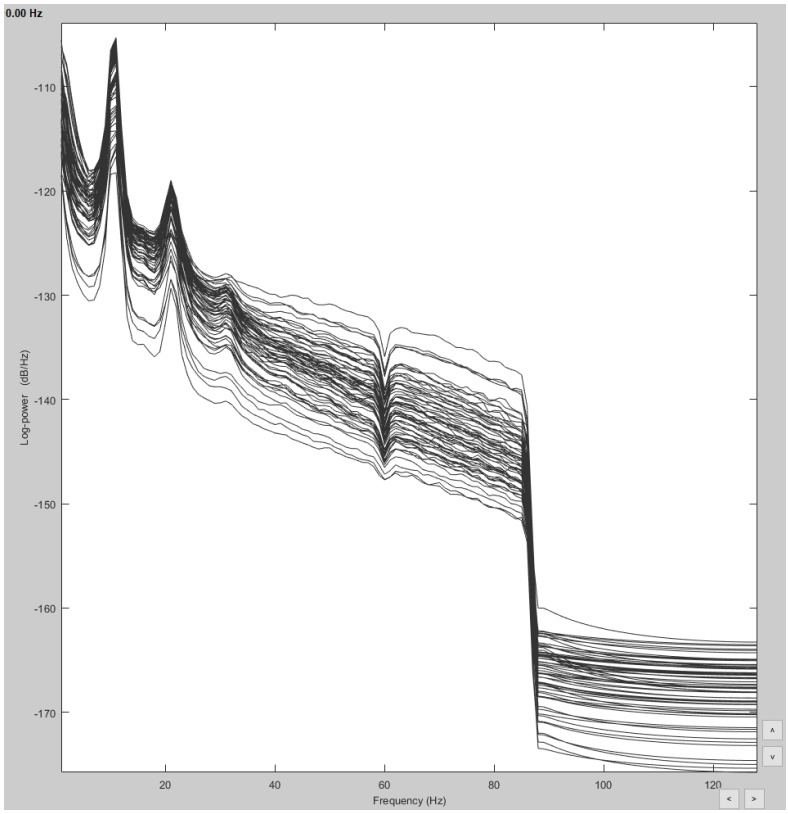

Figure 1.7: PSD after the application of Band Pass Filter on EEG data. The x-axis represents frequency in Hz and Y-axis represents log-power in dB/Hz.

Moreover, for the analysis of EEG signals, we need to reduce the frequency range by applying a bandpass filter. Figure 1.7 illustrates the PSD after the application of a bandpass filter from 0.5 Hz to 80 Hz on EEG data. However, in general, EEG data are not completely cleaned from various noises even after applying different filters. It is necessary to utilize more advanced techniques to remove other artifacts, which are identified from different noise sources.

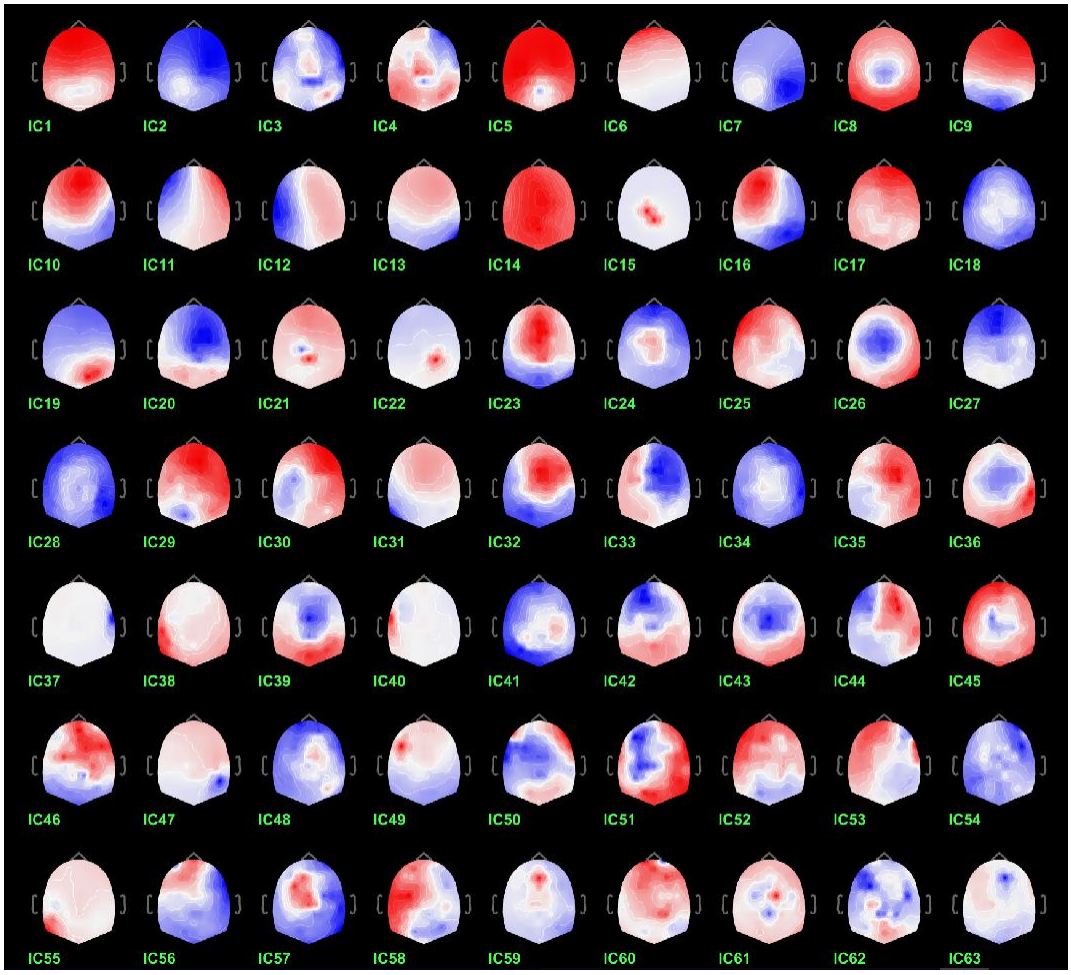

Figure 1.8: Independent Component Analysis for identifying different signal generating sources in the EEG data

The different signal generating sources in our data are analyzed and plotted by Independent Component Analysis (ICA) method in figure 1.8. An independent component from artifacts has a particular topography and frequency response. We need to identify those independent components and remove them. Once all the noises are eliminated from the data, we then segment the time series into different frequency bands for further analysis.

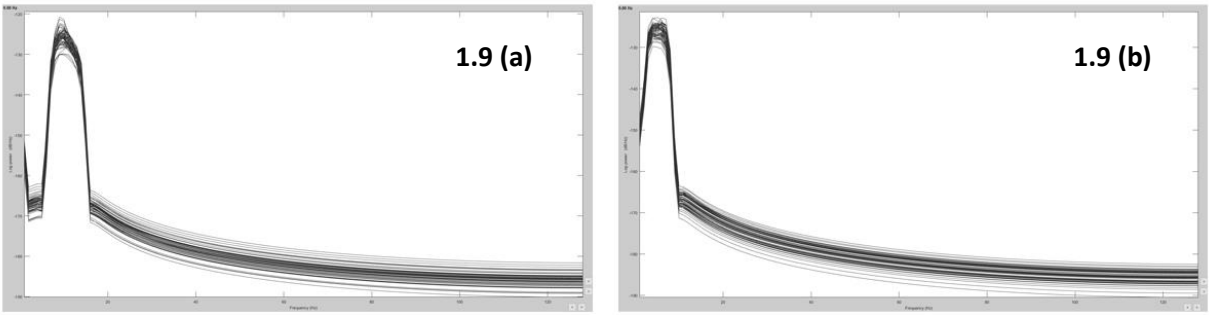

Figure 1.9: PSD of lower frequency bands. The PSD of the alpha band is illustrated in figure 1.9(a) and PSD of the theta band is illustrated in figure 1.9(b). The x-axis represents frequency in Hz and Y-axis represents log-power in dB/Hz

In general, a time series of EEG data has a broadband range of frequencies from 0.5 Hz to 80 Hz. The bandpass filter is applied to separate the EEG data into different frequency bands. Different frequency ranges are delta band (0.5 Hz to 4 Hz), theta band (4 Hz to 8 Hz), alpha band (8 Hz to 13 Hz), beta band (13 Hz to 30 Hz), and gamma band (30 Hz to 80 Hz).

1.4 Goal of this study

TPBM has shown its potential in recent studies as a potential therapeutic modality. It can improve the synaptogenesis and neurogenesis in the brain [16]. Moreover, no drug has been used to date to benefit neurodegenerative disorders [29]. Many studies have reported the improvement of cognition and memory in the animal models by the use of TPBM [15, 16]

There are a fewer number of studies performed to understand the underlying mechanism of photon propagation in the human tissue. I wanted to address these loopholes and bridge the gap by finding a solution experimentally. In the first aim, I analyzed the dependence of fluence of 1064-nm laser within brain tissue phantoms on several setup

parameters. These parameters included the power, aperture size, and detector distance, of the laser.

My second aim of this study was to investigate the changes in the human brain network caused by TPBM, measured by 64-channel EEG. To the best of our knowledge, no study has been done to investigate this phenomenon. The EEG device recorded the electrophysiological activity of the human brain with high temporal resolution and allowed the signals to be analyzed in different frequency bands. Understanding the underlying mechanism of the human brain network can enable us to detect early onset/stage of the neurodegenerative diseases [30]. This study helped me determine the statistically significant changes in the lower-frequency oscillation bands of the brain network caused by TPBM.

CHAPTER 2

INTERACTION BETWEEN THE 1064NM LASER AND HUMAN TISSUE PHANTOM

2.1 Introduction

There are many studies which have utilized different wavelengths of NIR laser [19, 31-35]. However, from an engineering and technical standpoint, there has been a very limited number of studies, regarding the light fluence at different penetration depth from a large-sized light or laser source. In this chapter, my focus was on the investigation of the relationship between 1064-nm laser energy delivered with different parameters and optical fluence at different penetration depth. These parameters included: (a) optical fluence as a function of laser beam size, (b) optical fluence as a function of laser power, and (c) optical fluence as a function of change in detector distance. For your convenience, I list the overall experimental setup parameters, as follows:

Experiment	Light	Power (W)	Aperture radius (cm)	Depth (cm)	Absorber
1	Laser; 1064 nm	0.5-4.5 In a step of 0.5	0.5 , 1.0, 1.5, 2.0, and 2.1 (no cap)	1.7	Ink; blood
2	Laser; 1064 nm	3.4	0.5, 0.75, 1.0, 1.25, 1.5, 1.75, 2.0, and 2.1 (no cap)	1.6 to 4.0	Ink; blood
3	Laser; 1064 nm	3.4	0.75, 1.0, 1.25, 1.5, 1.75, and 2.0	1.6 to 4.0	Ink; blood

Table 1: Different sets of laboratory experiments performed using the tissue phantom.

Specifically, tissue phantoms were used to perform several laboratory experiments where the optical fluence was measured and analyzed accordingly. In table 1, three types of

experimental results were obtained, namely, optical fluence as a function of (a) laser power, (b) laser beam size, and (c) penetration depth.

2.2 Materials and Methods

2.2.1 Instrumentation and setup

My aim was to study 1064 nm laser using different tissue phantoms that consisted of intralipid with either ink or horse blood to be used with 1064-nm laser. Intralipid was chosen to mimic light scattering in the human tissue, and ink or horse blood was used to act as absorbers in the tissue. Preference to choose two different light absorbers was dependent on the type of study. At different wavelengths, the horse blood had variable photon absorption, which is in contrast with ink's relative flat spectral response. After having made a liquid phantom solution with certain absorption and scattering properties, I measured the reduced scattering coefficient, μ_s', and the absorption coefficient, μ_a, using an ISS oximeter at 750 nm.

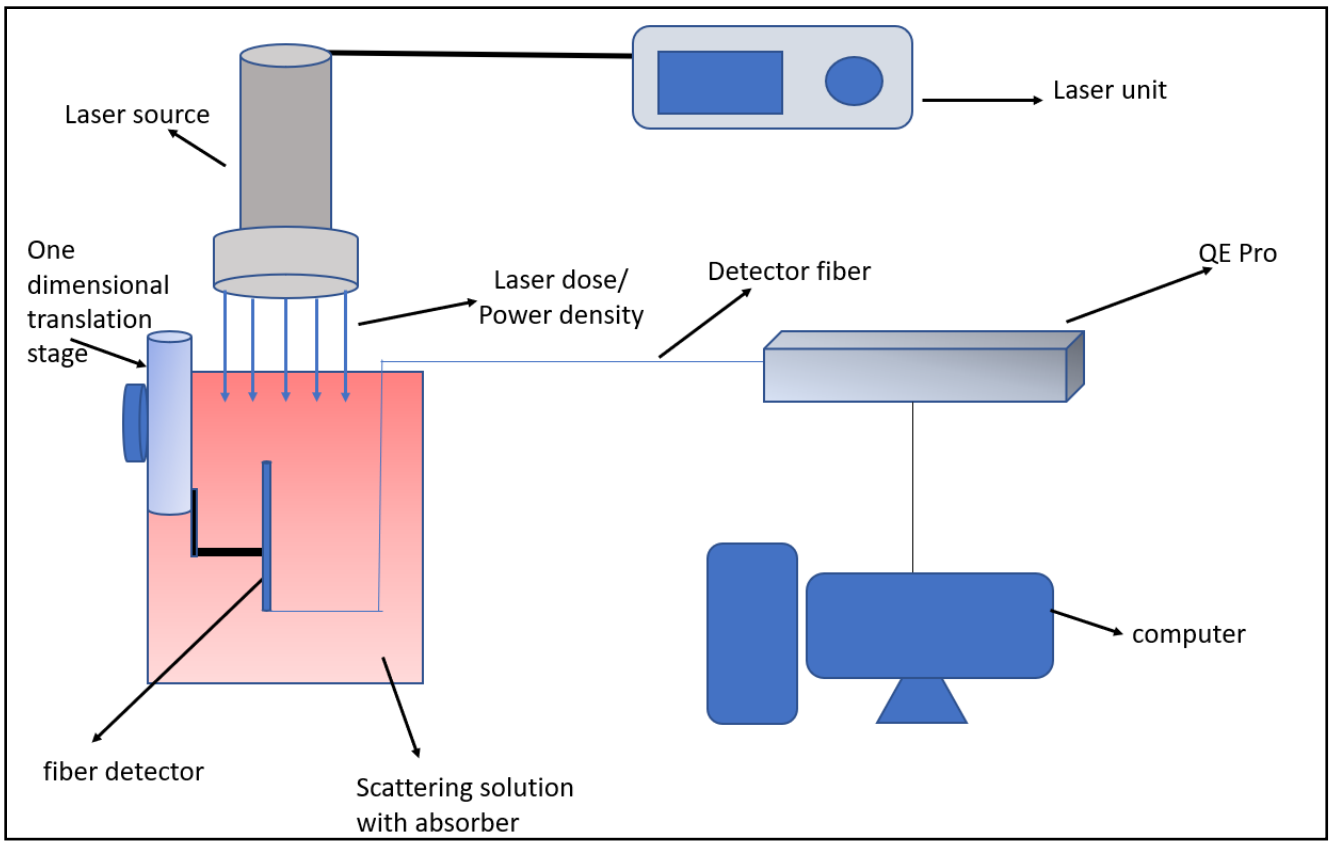

Figure 2.1: Basic setup of instrumentation and laboratory experiments. The laser source delivers an optical dose above the tissue phantom. An optical fiber Immersed within the liquid phantom serves as a detector right below the laser aperture and can be vertically translated in one-dimensional direction through a translation stage. For signal acquisition, the detector fiber is connected to a QE-Pro spectrometer, which is linked to a computer through the USB port.

Detailed setup for instrumentation and laboratory experiments is illustrated in figure 2.1. The laser source was placed and administered above the tissue phantom solution. To detect the light energy density or fluence, a 400-µm optical fiber was attached to a one-dimensional translation stage and placed within the intralipid solution. Other parts of instrumentation in the setup included a CCD spectrometer (QE pro, Ocean Optics, FL), with an input and output port. The input port received optical signals from the detector fiber; the output port of the QE Pro sent the converted electrical signals to the computer through a USB port. For data aqucision

and visulization, Ocean View software was used for real time display and for continous data recording of measured photons.

2.2.2 Experiment for phantom study

2.2.2.1 Setup to investigate effects of laser power density on optical fluence

From this set of study, I wanted to investigate the relationship of measured laser fluence within the phantom as a function of delivered optical power and aperture size in two separate solutions (i.e., with ink and horse blood). The first phantom solution was made with intralipid and ink having the reduced scattering coefficient of μs' = $10\ cm^{-1}$ and the absorbance coefficient of μa =$0.10\ cm^{-1}$, which were measured at 750 nm by the ISS oximeter. The second solution was made with intralipid and the horse blood having the same reduced scattering coefficient of μs' = $10\ cm^{-1}$ and the absorbance coefficient of μa =$0.10\ cm^{-1}$ at 750 nm. Other setup or experiment conditions are listed below.

Experiment	Light	Power (W)	Aperture radius (cm)	Depth (cm)	Absorber
1	Laser; 1064 nm	0.5-4.5 In a step of 0.5	0.5, 1.0, 1.5, 2.0, and 2.1 (no cap)	1.7	Ink; blood

Table 2: Experiment protocol for investigating the effects of laser power density on optical fluence. (Taken from table 1)

In this experiment, with the first solution, the detector fiber and 1064-nm laser were held at a fixed distance. To determine the linearity of detected optical fluence at a given depth or with different aperture size, the original 1064-nm laser aperture was covered by masks having different radius. The mask sizes ranged from 0.5 cm to 2.1 cm in radius, with a step size of 0.25

cm. Moreover, for every single aperture size, the optical fluence was measured when the laser power at the phantom surface was varied from 0.5 watts up to 4.5 watts with a step size of 0.5 watts.

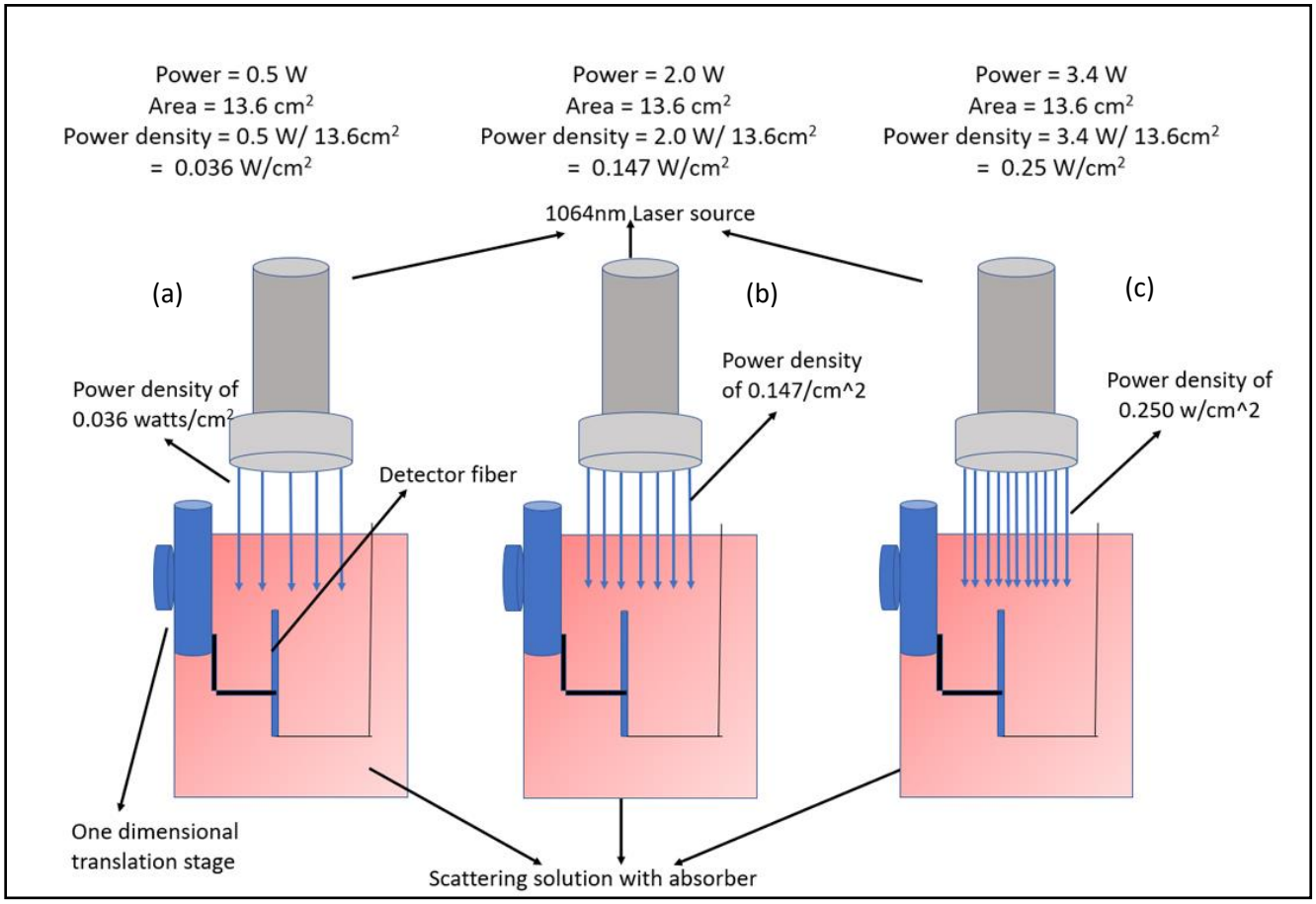

Figure 2.2: Experimental setup for 1064-nm laser with different light power densities. The increased number of lines with arrows from left to right represent increased optical power densities. The laser power density was calculated by the chosen laser power divided by the aperture area. The power densities in cases from the left to right panel are: (a) 0.036 w/cm^2, (b) 0.147 w/cm^2, and (c) 0.250 w/cm^2.

The setup using the 1064-nm laser with different laser power densities is illustrated in figure 2.2. The laser power was set through the laser setup unit with a range of 0-5 W, which was an upper limit for human studies, as reported by previous publications [36-39]. In this set of experiments, the laser aperture was fixed to be 13.6 cm^2, which allowed us to quantify laser

power density, as marked in Fig. 2.2. Accordingly, the power density given in Fig. 2.2(a) was 0.036 w/cm^2 with less dose delivered to the phantom solution, as indicated by a fewer number of arrows. In Fig. 2.2(b), the power density was increased to 0.147w/cm^2, depicted by more arrows. In Fig. 2.2(c), the power density of laser was 0.250 w/cm^2.

2.2.2.2 Setup to investigate effects of laser beam size on light fluence

I was interested in investigating the effects of different aperture sizes on the optical fluence received within the tissue phantom at different depths. For this study, the power of 1064-nm laser was fixed at 3.4 watt; the laser aperture was placed at a fixed distance of 2 cm above the tissue phantom surface. For each set of readings at a particular aperture size, detector fiber was displaced vertically inside the tissue phantom solution. It was translated vertically through a one-dimensional translation stage, to detect the fluence of signal at different depths.

Experiment	Light	Power (W)	Aperture radius (cm)	Depth (cm)	Absorber
2	Laser; 1064 nm	3.4	0.5, 0.75, 1.0, 1.25, 1.5, 1.75, 2.0, and 2.1 (no cap)	1.6 to 4.0	Ink; blood

Table 3: Experiment protocol for investigating the effects of laser beam size on optical fluence. (Taken from table 1)

The first set of experiment was taken with a cap having a 0.5 cm radius aperture in the middle. Gradually for each set of reading, the aperture size using different mask caps was increased by a step size of 0.25 cm until the largest cap having an aperture of 2.1 cm. The tissue phantom solution had μs' = 10 cm^{-1} and μa =0.10 cm^{-1} made of intralipid and ink. The second solution with the same μs' = 10 cm^{-1} and μa =0.10 cm^{-1} was prepared using intralipid and horse blood.

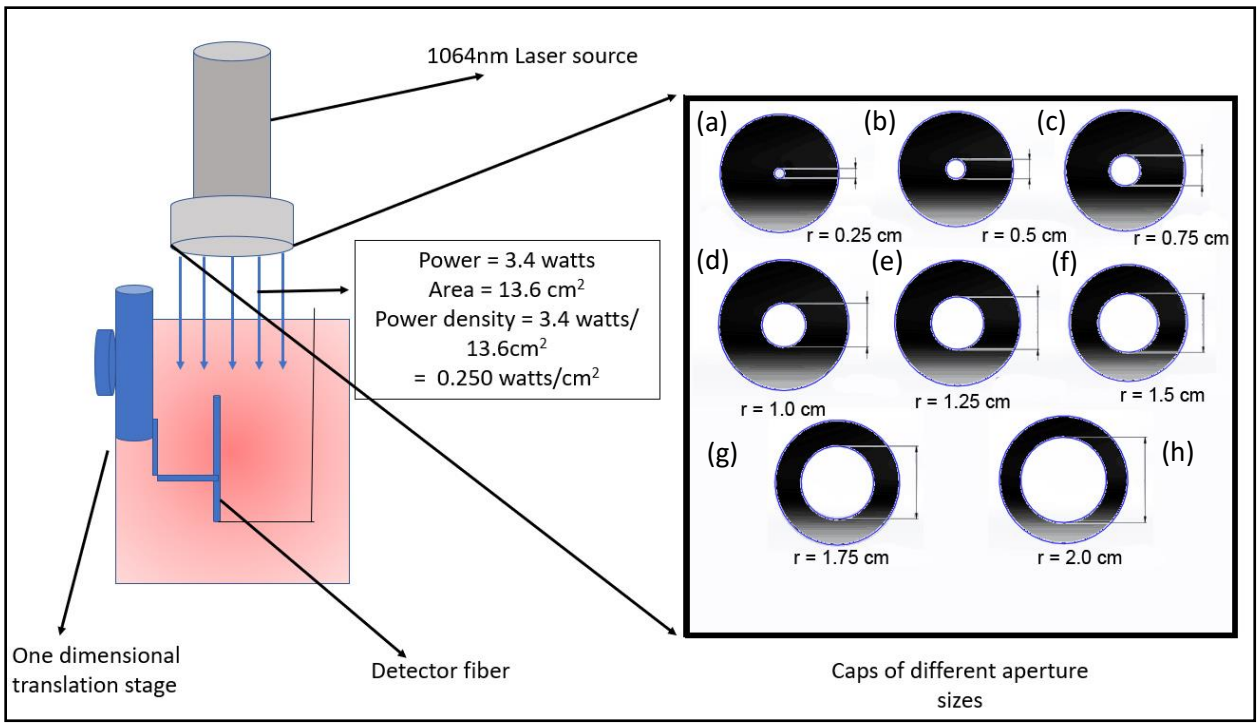

Figure 2.3: 1064 nm laser is shown delivering laser dose to the tissue phantom solution with a fix power of 3.4 watts. Different caps having variable aperture sizes in the middle are shown on the right-hand side, which are: (a) 0.25 cm aperture, (b) 0.50 cm aperture, (c) 0.75 cm aperture, (d) 1.0 cm aperture, (e) 1.25 cm aperture, (f) 1.50 cm aperture, (g) 1.75 cm aperture, and (h) 2.0 cm aperture. These caps are placed on the 1064 nm laser source head for each set of experiment.

Setup for analyzing the relationship between optical fluence and the laser beam size is illustrated in Figure 2.3. Caps of different aperture sizes were placed on the laser head to change fluence at the output. Starting from the smallest cap with an aperture size of 0.25 cm, the cap was increased size by a step size of 0.25 cm, until the largest aperture size of 2.1 cm was used. Different aperture size caps are illustrated from (a) to (h).

2.2.2.3 Analytical solution from Green's Equation

For comparison between the experimental results and mathematical expression to estimate the laser beam size effects on the optical fluence, I performed diffusion-based calculation using Green's equation on MATLAB.

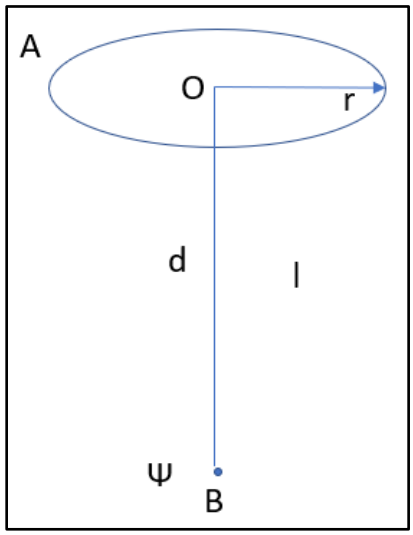

Figure 2.4: Optical signal received by the point detector 'B' from the 1064nm laser source center at point 'O'.

Mathematical equation for calculating the optical fluence at 'B' from a point source center 'O' is given by:

$$\Psi(d) = \frac{3\ \mu s\prime}{4л} * [e^{-(\mu eff * d)}/d], \qquad (2.1)$$

Equation 2.1, represents the Greens function to diffusion equation for an infinite scattering medium. μeff is the combined effect of absorption and scattering of the tissue phantom, which is $\sqrt{3 * \mu s' * \mu a}$. The distance between source center point 'O' and the point detector 'B' is represented by *d*.

Specifically, the actual reduced scattering coefficient and the absorption coefficient observed in the experiments were the input parameters for numerical calculations for comparison. Our experiment had a wider aperture or area of laser source, and detector cable was considered as a point source.

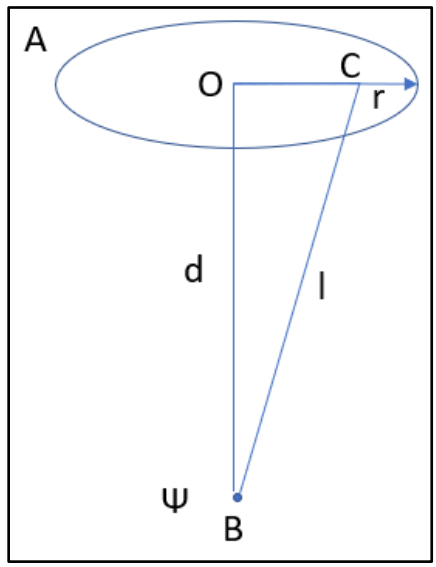

Figure 2.5: Optical signal or fluence received by the point detector from the point source at 'C' on the 1064 nm laser source.

In figure 2.5, the point source is now at point 'C'. Mathematical equation for calculating the optical fluence at 'B' from 'C' will be:

$$\Psi(r) = \frac{3\ \mu s\prime}{4л} * \left(\frac{e^{-(\mu eff * l)}}{\sqrt{r^2 + d^2}}\right) r\ dr\ d\Theta, \qquad (2.2)$$

Equation 2.2, represents the mathematical expression of optical signal received by the detector at 'B' from a particular point 'C' on the source. 'l' is the distance from 'C' to 'B' which is equivalent to l = $\sqrt{r^2 + d^2}$.

Theoretically, the solution of diffusion equation at distance 'B' from the source 'C', with optical properties of μs' and μa, and a radius, r, of the light source aperture, can be obtained by

integrating the area of the laser aperture over the Green's equation with respect to the radius of laser source. Mathematically it is represented as:

$$\Psi(l,A) = \frac{3\ \mu s\prime}{4л} * \int_0^{2\pi} d\,\theta \int_{area} \left(\frac{e^{-\left(\mu eff*\sqrt{r^2+d^2}\right)}}{\sqrt{r^2+d^2}}\right) r\,dr\,, \qquad (2.3)$$

The final expression after integration over the aperture is given below:

$$\Psi_B = \frac{3\ \mu s\prime}{2\mu eff} * \left[e^{-(\mu eff*d)} - e^{-\left(\mu eff*\frac{\sqrt{R^2+d^2}}{1}\right)}\right]. \qquad (2.4)$$

For estimating the effect of illumination area on the optical fluence, the analytical solution, equation 2.4, can be compared.

2.2.2.4 Setup to investigate effects of penetration depth on optical fluence

In this experiment, I wanted to analyze the effect of penetration depth on the optical fluence under similar conditions using 1064-nm laser.

Experiment	Light	Power (W)	Aperture radius (cm)	Depth (cm)	Absorber
3	Laser; 1064 nm	3.4	0.75, 1.0, 1.25, 1.5, 1.75, and 2.0	1.6 to 4.0	Ink; blood

Table 4: experimental protocol for analyzing the effect of penetration depth on the optical fluence. (Taken from table 1)

Different tissue phantom solutions, which had identical μs' and μa at 750 nm for both, were used. The first solution was made using intralipid and ink, which had μs' = 10 cm^{-1} and μa

= 0.10 cm^{-1}. The second solution was made from intralipid and the horse blood, which also had $\mu s' = 10\ cm^{-1}$ and $\mu a = 0.10\ cm^{-1}$.

As represented in table 4, the experimental protocol included the displacement of detector fiber with each aperture size. The 1064-nm laser source was masked with caps having different aperture sizes. Starting from r=0.75 cm aperture, the distance of detector was varied in order to observe the effect of photon penetration on the optical signal/fluence. The distance of detector fiber was varied using a one dimensional translation stage. Each time the aperture was increased by a step radius size of 0.25 cm for different set of experiments, until the largest aperture radius size of 2.0 cm was used.

2.2.3 Data analysis

For each set of experiments, the intensity of photon count at each wavelength was acquired utilizing an ocean view software. To estimate the optical fluence for different sets of experiments, all the intensities under the spectral bandwidth from 1034 nm to 1094 nm were integrated to obtain the optical fluence.

2.3 Results

2.3.1 Power-dependent optical fluence (Experiment 1)

This set of experiment helped understand the effect of 1064-nm laser power on the optical fluence, at a fixed depth. Experiment results are presented in Fig. 2.6(a) with ink solution, and Fig. 2.6(b) with horse blood.

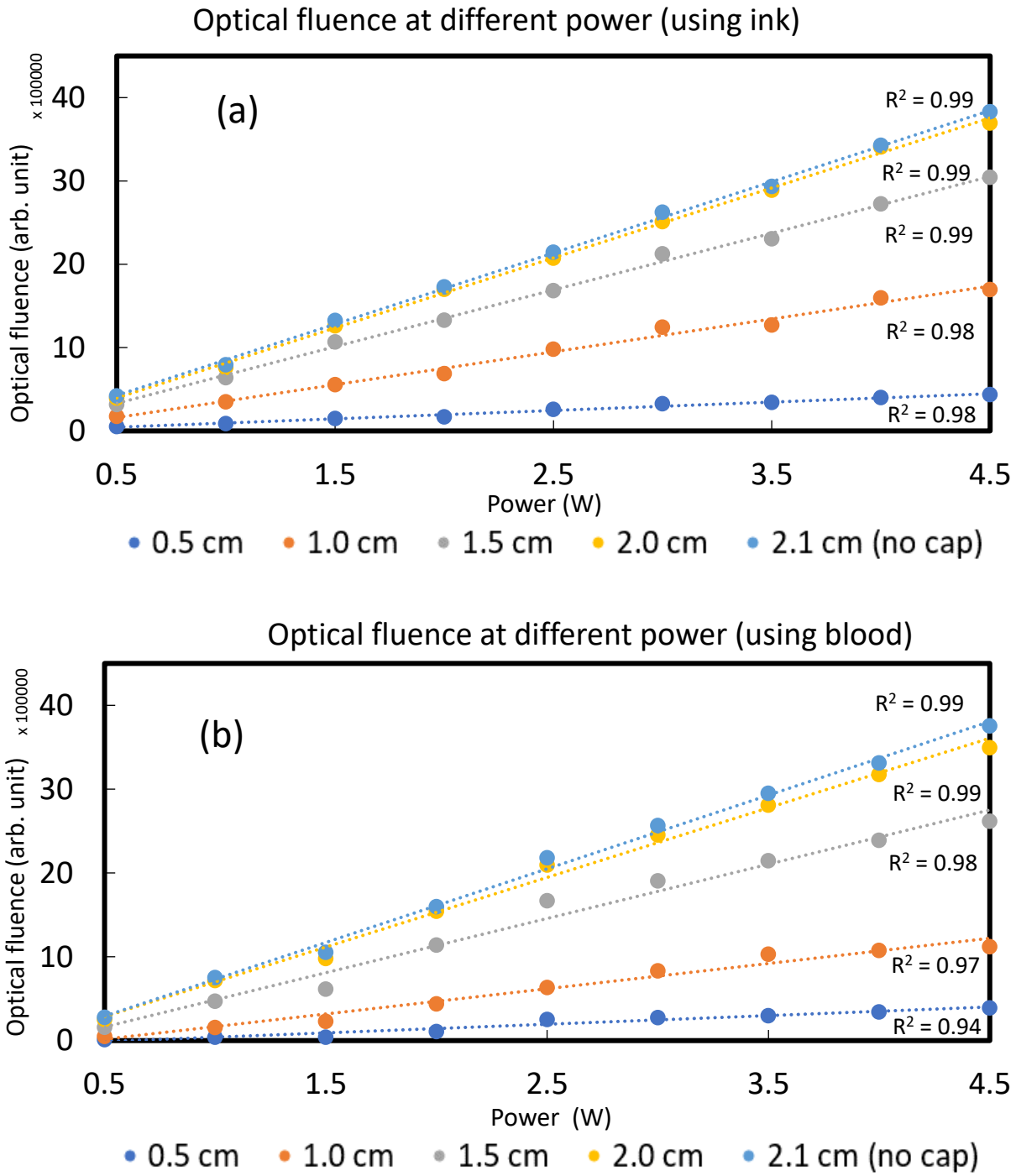

Figure 2.6: The relationship of optical fluence and 1064-nm laser power, utilizing different aperture sizes. The x-axis represents irradiance or laser power in watts and y-axis represents optical fluence. Readings were taken from two different tissue phantom solutions, that are composed of different absorbers: (a) ink and (b) blood.

For this study, first set of experiments were performed using a 0.5 cm radius mask cap. The power of 1064-nm laser was varied; optical fluence at a penetration depth of 1.7cm was determined. At a fixed aperture size, the relationship between the optical fluence and power of 1064-nm laser was found to be very linear.

For the reproducibility of results, a series of experiments were performed utilizing different mask caps with an aperture of 1.0 cm, 1.5 cm, and 2.0 cm. From each set of experiment, a perfect linear relationship between the laser power and optical fluence was found to be consistent.

2.3.2 Aperture-dependent optical fluence (Experiment 2)

From this set of study, I wanted to observe the effect of the laser beam size on the optical fluence. The mathematical solution with experimental data under similar conditions were compared at a fix penetration depth.

To determine the optical fluence (OF) at a fixed distance numerically, Green's equation for a sized light source (eq 2.4) was used. The experimental portion included the tissue phantom solutions that were made using different absorbers.

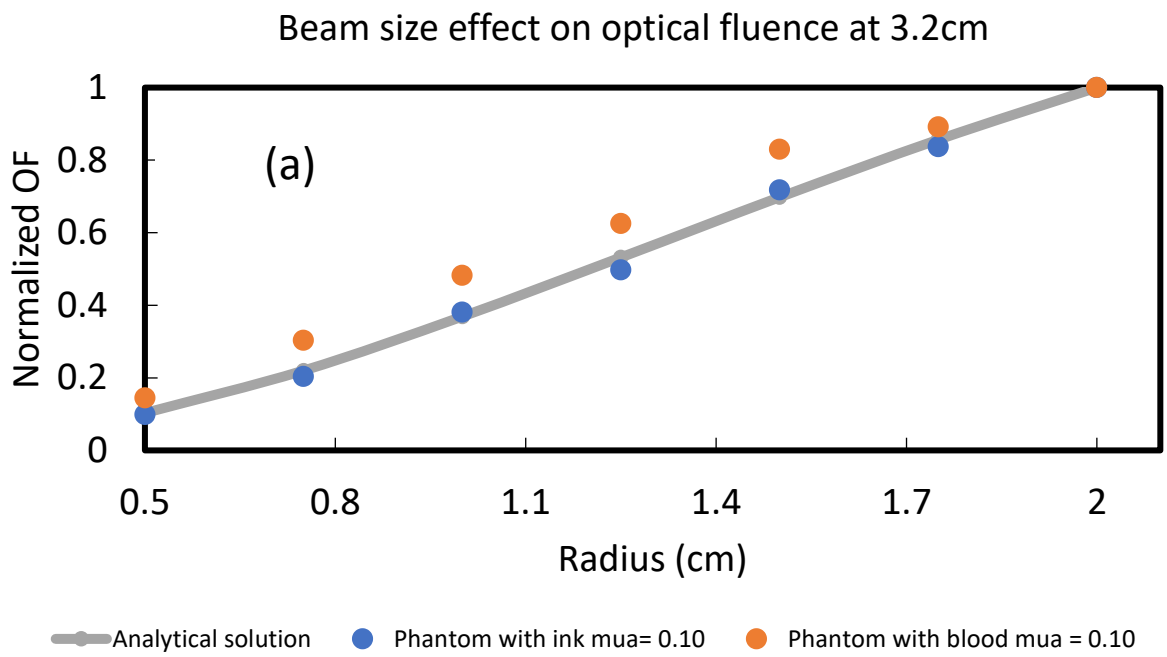

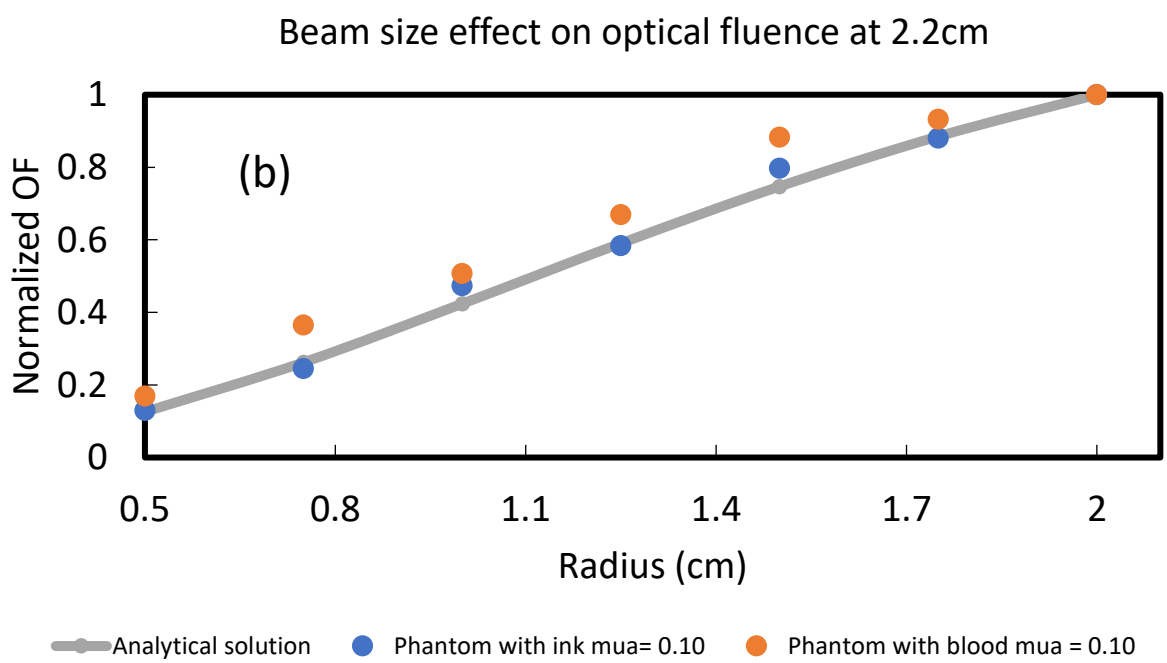

Figure 2.7: Relationship between the beam size of 1064-nm laser and normalized optical fluence at a fix depth. The x-axis represents the radius in cm and y-axis represents normalized optical fluence. The analytical solution is obtained from eq 2.4. The experimental data is acquired from two different tissue phantom made with (a) ink and (b) blood at μ_a = 0.10 cm^{-1}. The experimental readings are taken at a penetration depth of (a) 2.2cm and (b) 3.2cm.

In this study, the optical fluence was analyzed at different penetration depths, namely at 2.2 cm and at 3.2 cm. It is clear that optical fluence received with different aperture size of 1064-nm laser illumination was very consistent with the analytical solution for both blood and ink experiments.

2.3.3 Depth-dependent optical fluence (experiment 3)

For this study, I wanted to observe optical fluence at different penetration depths, utilizing different aperture sizes. The experimental results were compared with the analytical solution obtained from eq 2.4, at different penetration depths.

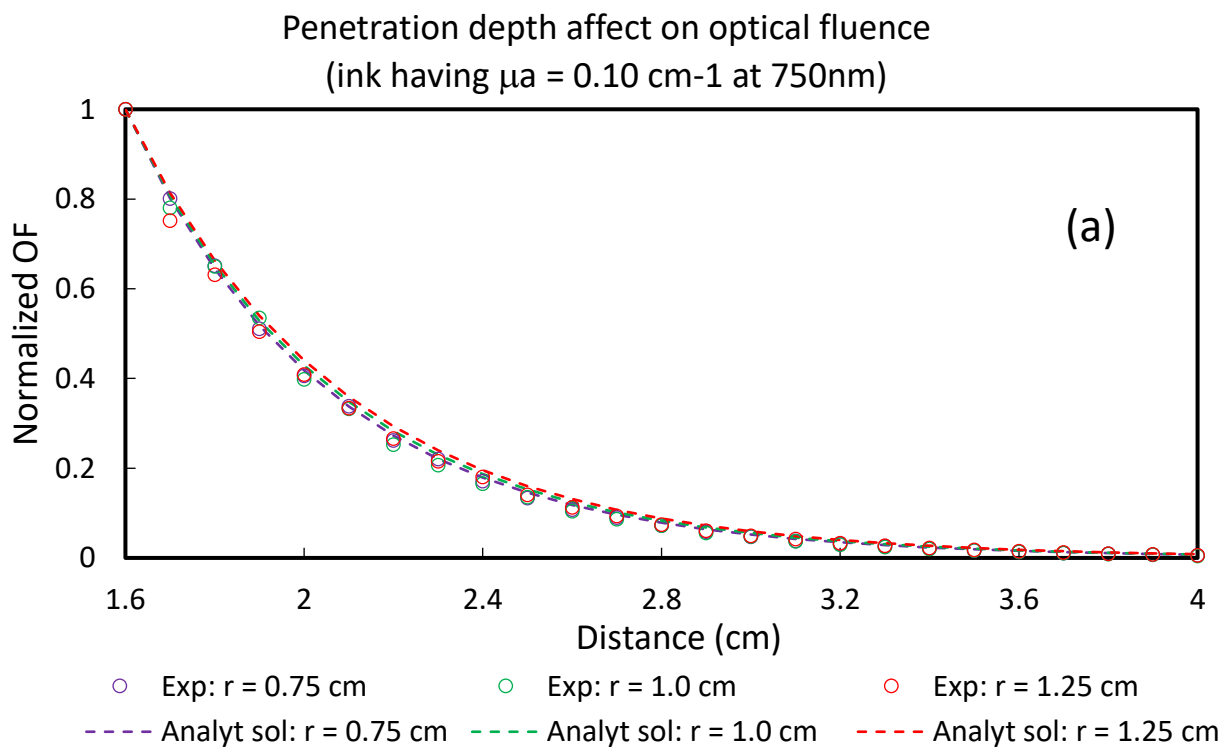

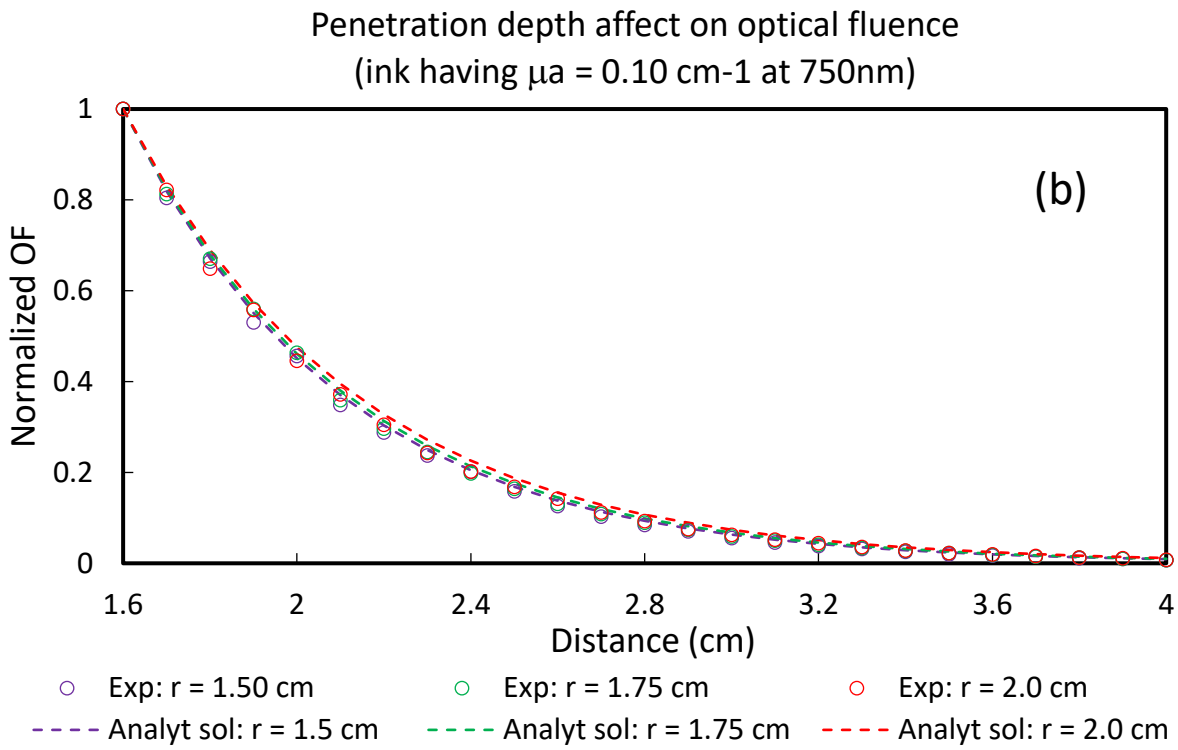
Penetration depth affect on optical fluence
(ink having μa = 0.10 cm-1 at 750nm)
(b)
Normalized OF
Distance (cm)
1
0.8
0.6
0.4
0.2
0
1.6
2
2.4
2.8
3.2
3.6
4
Exp: r = 1.50 cm
Exp: r = 1.75 cm
Exp: r = 2.0 cm
Analyt sol: r = 1.5 cm
Analyt sol: r = 1.75 cm
Analyt sol: r = 2.0 cm

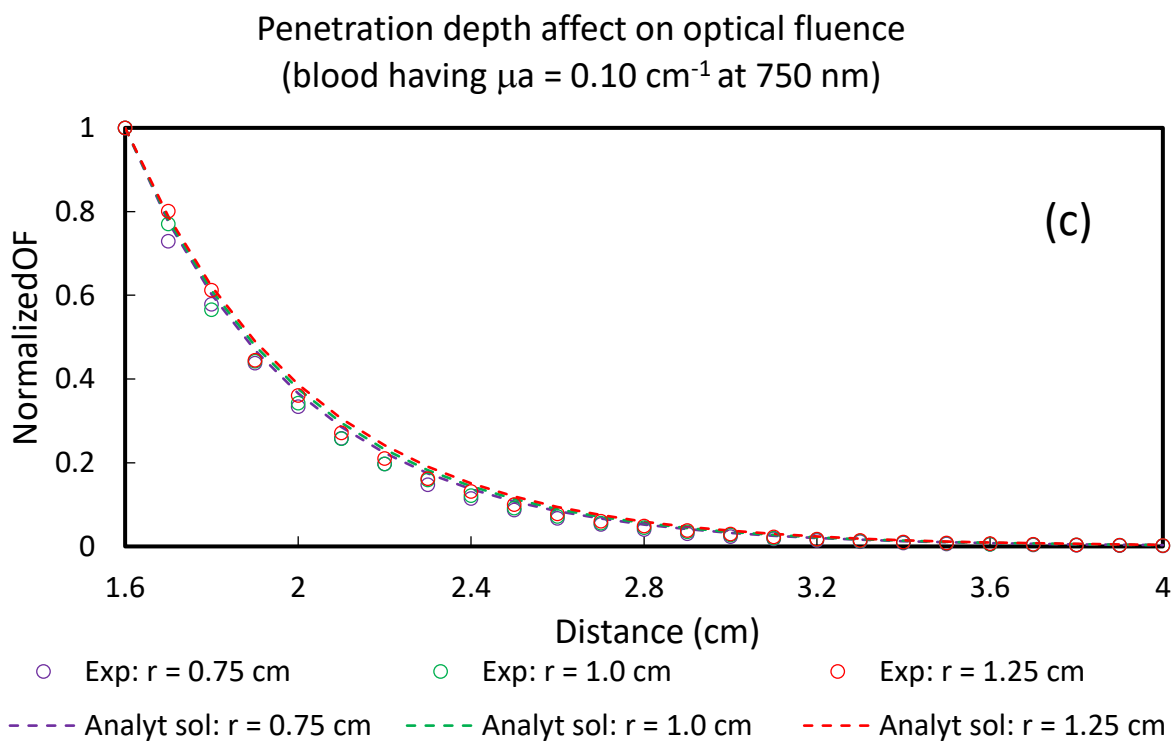
Penetration depth affect on optical fluence
(blood having μa = 0.10 cm-1 at 750 nm)
(c)
NormalizedOF
Distance (cm)
1
0.8
0.6
0.4
0.2
0
1.6
2
2.4
2.8
3.2
3.6
4
Exp: r = 0.75 cm
Exp: r = 1.0 cm
Exp: r = 1.25 cm
Analyt sol: r = 0.75 cm
Analyt sol: r = 1.0 cm
Analyt sol: r = 1.25 cm

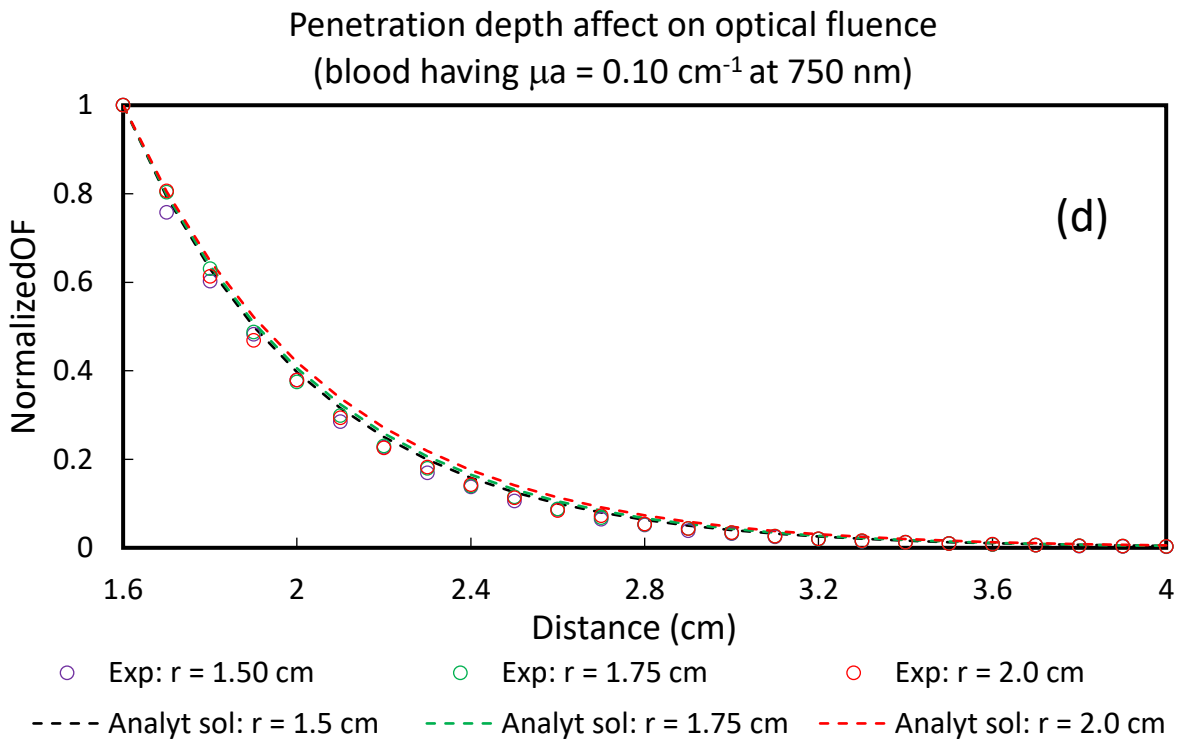

Figure 2.8: Relationship between the penetration depth and normalized optical fluence utilizing different beam sizes. The x-axis represents the distance in cm and y-axis represents normalized optical fluence. Analytical solution is determine using eq. 2.4, and it is plot with experimental results: (a, b) tissue phantom with ink and (c, d) tissue phantom with blood, at 0.10 cm^{-1}.

From figure 2.8, The measured fluence is decaying for all three conditions. Overall, the experimental data are matched well with the analytical solution for different set of aperture sizes. Note that the μa value at 1064 nm for blood was estimated based on that of HbO concentration at 750 nm. A standard spectrum of extinction coefficients of HbO was used for this estimation.

2.4 Discussion

For many decades, PBM has been extensively used for the treatment of pain and wound healing [4, 12, 13, 15, 16, 19-21]. However, there are only fewer studies done to understand the underlying mechanism of photon propagation with sized beams at different power in the

human tissue. In order to bridge this gap and propose a solution, three different sets of experiments were performed on tissue phantoms utilizing the 1064-nm laser source.

2.4.1 Optical fluence as a function of power

Effectiveness of PBM is dependent on the power density and laser dose [39]. From the first set of experiments, my aim was to study the relationship of laser power versus optical fluence. It has been observed that the optical fluence at a fixed depth is linearly proportional to the power of illumination. The linearity between the optical fluence and power for the 1064-nm laser source is independent of the beam size and type of absorber used, at a fix penetration depth.

Two important findings can be reported from this study:

1. Optimal power of 1064-nm laser required for photon propagation in different applications can be evaluated from the linear relationship.
2. Deep regions of the brain tissue phantoms can be reached by estimating the required power for each beam size of the laser source.

2.4.2 Optical fluence as a function of laser beam size

Many studies involving PBM do not report the area of laser beam [40-42]. It is a very important parameter that determines its stimulation efficiency [39]. My aim was to study the relationship of the optical fluence and area of illumination. It has been observed from fig 2.9 that an increase in the area of illumination of laser results in a significant increase in the optical fluence, as shown in analytical and experimental data at a given depth.

Two important findings can be reported from this study:

1. A larger radius of 1064-nm laser should be used for more optical fluence at a fix penetration depth.
2. Effective stimulation requires a larger radius of the laser source to deliver more photons at a fix power.

2.4.3 Optical fluence as a function of penetration depth

For my third set of study, I investigated the effect different penetration depths on optical fluence. It has been observed that the optical fluence, from both analytical and experimental data, decreases with the increase in penetration depth.

Two important findings can be reported from this study:

1. The decay curves from both ink and blood phantoms match well with the analytical solution (eq 2.4), which can be utilized for estimating the μeff.
2. By estimating the optical fluence at different penetration depths, laser dose can be delivered to the different regions of the brain with precision.

CHAPTER 3

INVESTIGATION OF BRAIN NETWORK CONNECTIVITY INDUCED BY TRANSCRANIAL PHOTO BIOMODULATION IN HUMAN SUBJECTS

3.1 Introduction

The analysis of brain networks can identify the early onset of many neurological disorders [30]. For this aim, I am going to investigate the changes in brain network caused by transcranial photo biomodulation (TPBM) using 1064-nm laser. My focus will be analyzing the lower frequency bands of the brain network to determine the significant changes caused by TPBM.

3.1.1 Functional connectivity estimation on EEG Data:

Based on the previous studies [37, 43], CCO activity was increased with an increase in the PBM dose. It could lead to a hypothesis that neuronal activity and network could be modulated and activated by TPBM.

In this study, electrophysiological brain signals are recorded using 64 channel EEG system by my colleagues, Dr. Xinlong Wang, Mr. Sahil S Nalawade , and Ms. Divya D Reddy. This modality has a high temporal resolution and it gives the flexibility to perform analysis on different frequency bands [27]. Each frequency band of EEG signal has its own importance and significance when it comes to analyzing and interpreting the signals [27].

There are multiple methods to process and analyze pre-processed EEG signals to study functional connectivity of the brain networks [27, 44]. It can be very difficult to select an

appropriate functional connectivity method for EEG signals and there is no ideal method to calculate functional connectivity of brain networks through EEG signals [44, 45].

I have opted to calculate functional connectivity through Pearson correlation coefficient(r) obtained from the amplitude between 2 signals in the time domain. It is the most common and straight forward method to calculate functional connectivity parameter [27, 44]. Recent studies have used Pearson Correlation coefficient (r) method for calculating functional connectivity over a longer interval of time for the same frequency band [45-47]. This correlation technique has a higher sensitivity to the coupling parameter resulting in better performance [45]. For this study, I wanted to calculate functional connectivity over long interval time window and observe changes induced by TPBM on the brain networks.

3.2 Materials and Methodology:

3.2.1 Participants

Healthy Subjects with no serious medical conditions and having an average age of 31 with standard deviation of (+- 13 years), were recruited from the general population of students at the University of Texas at Arlington. Each subject underwent 2 days of experiments, placebo on the first day and laser stimulation on the second day.

This study was reviewed and approved by the Institutional Review Board (IRB) of the University of Texas at Arlington (UTA). Experiments were carried out following the framework set by NIH, and other federal agencies. Ethical guidelines and protocols were according to the guidelines set by IRB UTA for conducting experiments on human subjects. Written consent from each subject was obtained prior to this study.

3.2.2 Instrumentation

NIR laser used in this study had a 1064-nm wavelength and approved for safe usage by the FDA. The beam of laser was collimated to avoid any undesired artifacts from the artificial noise and the laser area was consistent approximately around 13.6 cm^2. The laser dose was administered on subject's right forehead from a 2 cm distance.

In the placebo treatment group, laser had a reduced power of 0.1 W and aperture of 1064 nm laser was covered with a black cover. For the laser treatment group, the laser power and the power density were set to 2.2 W and 0.25 W/cm^2, respectively. Moreover, safe laser stimulation parameters were calculated as follows:

Total laser power = 2.2 W;

Area of laser beam radiation = 13.6 cm^2;

Power density was calculated to be = 2.2 W /13.6 cm^2 = 0.161 W/cm^2;

Each cycle radiated for 60 seconds, each cycle had total laser energy of = 2.2W x 60s = 132 J/cycle;

Each cycle had total laser energy density = 0.161W/cm^2 x 60 s = 9.66 J/cm^2/cycle.

Data was recorded at 256Hz sampling frequency using the 10-10 system arrangement utilizing 64-electrode Biosemi. This system had a higher channel density as compared to the traditional 10-20 system.

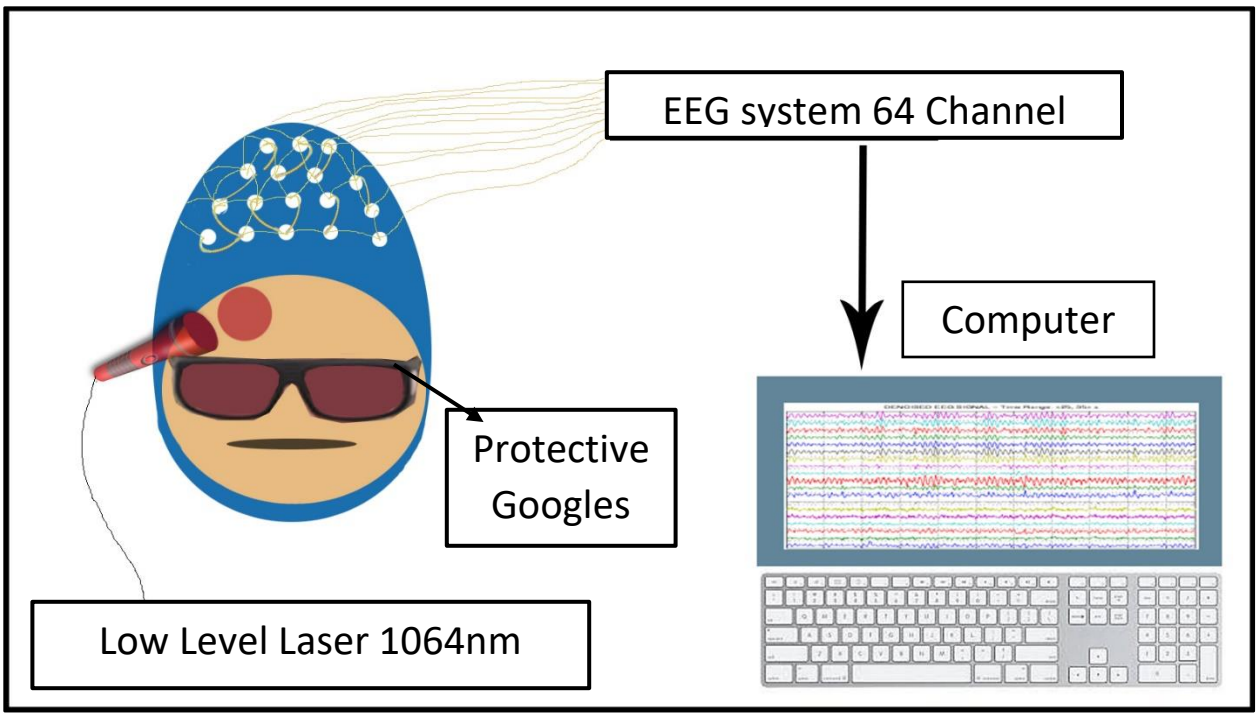

Figure 3.1: Schematic diagram of the experimental setup.

The experimental setup for this study is shown in fig. 3.1. The Instrumentation consists of a 1064-nm laser, biosemi system for eeg data acquisition, and the computer system. EEG cap having 64 electrodes was used to record electrophysiological acitivity from different locations of the human brain. Bio-semi module had 2 ports: input and output port. Input port was connected to 64 electrodes and output port had a direct interface with the computer system using the USB port. 1064-nm laser was administered on the right forehead of the subject and the electrophysiological signal was shown on the computer screen in real time. Furthermore, for safety purpose subject were given to wear protective goggles to protect eyes from the exposure of laser during the experiment.

3.2.3 Experiments

After each participant was comfortably seated, the EEG cap was placed on the subjects head and electrodes were attached. To decrease the resistance of electrical signals detected by the electrodes, EEG gel was used.

Experiment for two treatment groups were conducted on separate days. The block design of placebo and laser stimulation group is illustrated in figure 3.2. Each treatment group had 2 minutes of baseline at the resting state. Following baseline, laser treatment was adminsitered for 11 minutes which is followed by 3 minutes of recovery period.

It was a single blinded study, where subjects were unaware of the type of treatment they were receiving. Experiment was carried out on both treatment groups in a similar manner. Moreover, even in the placebo group the TILS laser unit was turned on, so the participants can hear the sound of the machine. However, the power was 0.1W and 1064nm laser source aperture was covered by a black cap. In laser stimulation group, total power of laser was 2.2W, which produced minimal amount of heat.

Experiment lab was specially designed to carry out laser study and only trained students were allowed to access it. Moreover, lab windows were covered with black cloths to minimize the exposure to external light. Experiment was carried out in a dark room to avoid any inteference with stray room light.

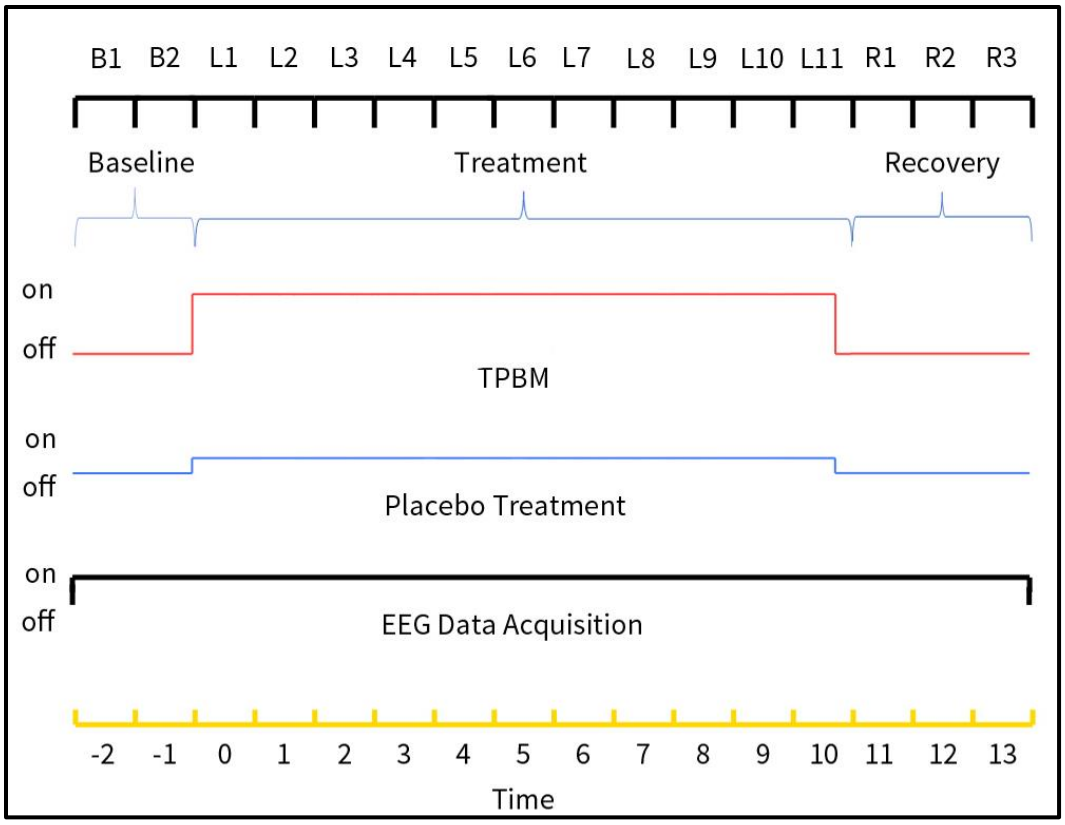

Figure 3.2: Block diagram of the experimental protocol

The experimental protocol is illustrated in figure 3.2. Starting two minutes is the baseline, which is indicated by flat region spanning from B1 till B2. At the start of L1 segment, the treatment was administered with precise timing and it was administered for 11 minutes up to L11. Recovery phase was the post stimulation period that lasted for 3 minutes, starting from R1 till R3. EEG data acquisition was turned on for the entire duration of experiment starting from B1 till R3.

3.2.4 Data processing and statistical analysis

The entire data processing steps are outlined in Fig. 3.3. Raw eeg data had artifacts and it needed filtering before the actual statstical analysis could be performed. For post pre-

processing, I used Brainstorm software which is a matlab based toolbox. EEG signal was prone to different types of noises and it needed filtering. Notch filter was applied at 60 Hz and 120 Hz to remove the main line noise from the EEG data, and then band pass filter was applied from 0.5 Hz to 80 Hz for the removal of different unwanted signals, such as DC offset, system slow drifts, and any higher frequencies.

Noises due to eye blinks, muscle movement, and heart pulsation signals had been removed using Independent Component Analysis (ICA). Following ICA analysis, data was epoched into different time segments. Due to settling time, the first minute data were excluded; namely, data within segment B1 were not used for further analysis**.** Starting from B2 up til R3, I segemented the 15 minutes data into fifteen 1-minute blocks. Moreover, in each block the broadband EEG signals (0.5-80 Hz) were filtered into 5 time series with 5 distinct frequency ranges: delta band (0.5-4 Hz), theta Band (4-7 Hz), alpha band (8-13 Hz), beta band (13-30 Hz), and gamma band (30- 80 Hz), using corresponding band pass filters. Next, temporal data acquired by each EEG channel under the laser/placebo stimulation were calibrated or normalized with respect to their averaged baselines, respectively.

Pearson correlation coefficient(r) was used to estimate the functional connectivity. I opted to use this technqiue due to its multiple advantages [27, 44-47]. The correlation coefficient for each of 15 blocks was calculated for each EEG channel in each individual frequency band using the Brainstorm software. Statistical analysis could not be performed on Pearson correlation coefficient(r), as it does not follow normal distrbution. Fisher transform technique was used to convert each set of data into normal distribution**.** Next, I carried out 2 sample T-Test across 20 subjects in both laser and placebo groups. To find regions or locations

on the scalp that exhibit significant differences in correlation coefficient (i.e., r) between the two cases, T-value of 2.03 was selected (corresponding to 95% confidence level) as the threshold to define the connectivity between the two scalp locations. All the T values which were smaller than 2.03 were threshold to be zero, meaning no connectivity between those locations.

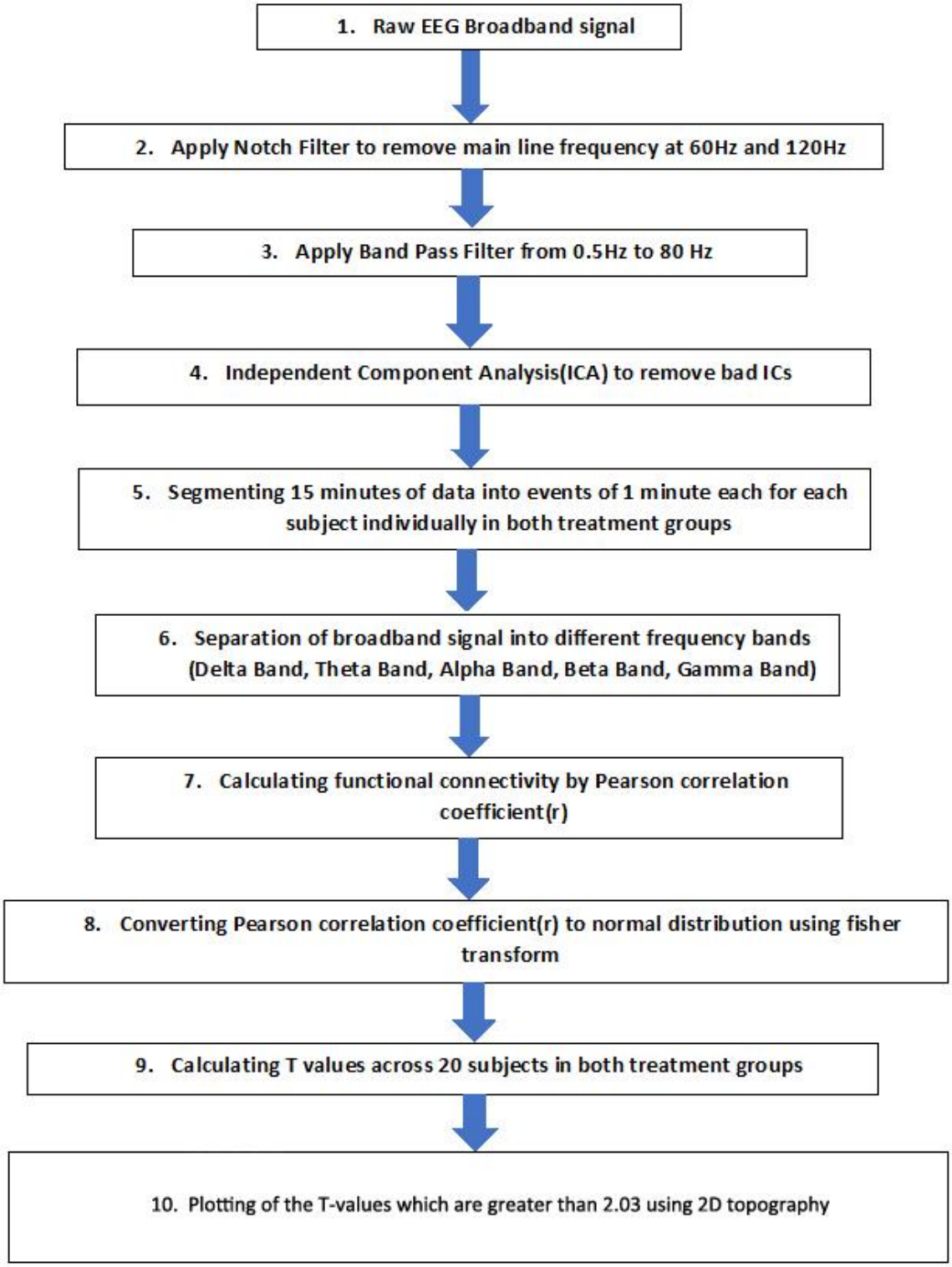

Figure 3.3: Flow chart describing detailed procedures of EEG Data post-processing.

3.3 Results

Two dimensional topographies of T-maps were plotted to observe overall connectivity patterns across regions over the entire scalp in theta band and alpha band, as shown in Fig. 3.4(a) and 3.4(b), respectively. These figures present T-maps throughout temporal segments of experiments in a step of 2 minutes: 1st min, 3rd min, 5th min, 7th min, 9th min, 11th min, and recovery :1st min, 2nd min and 3rd min.

(a)

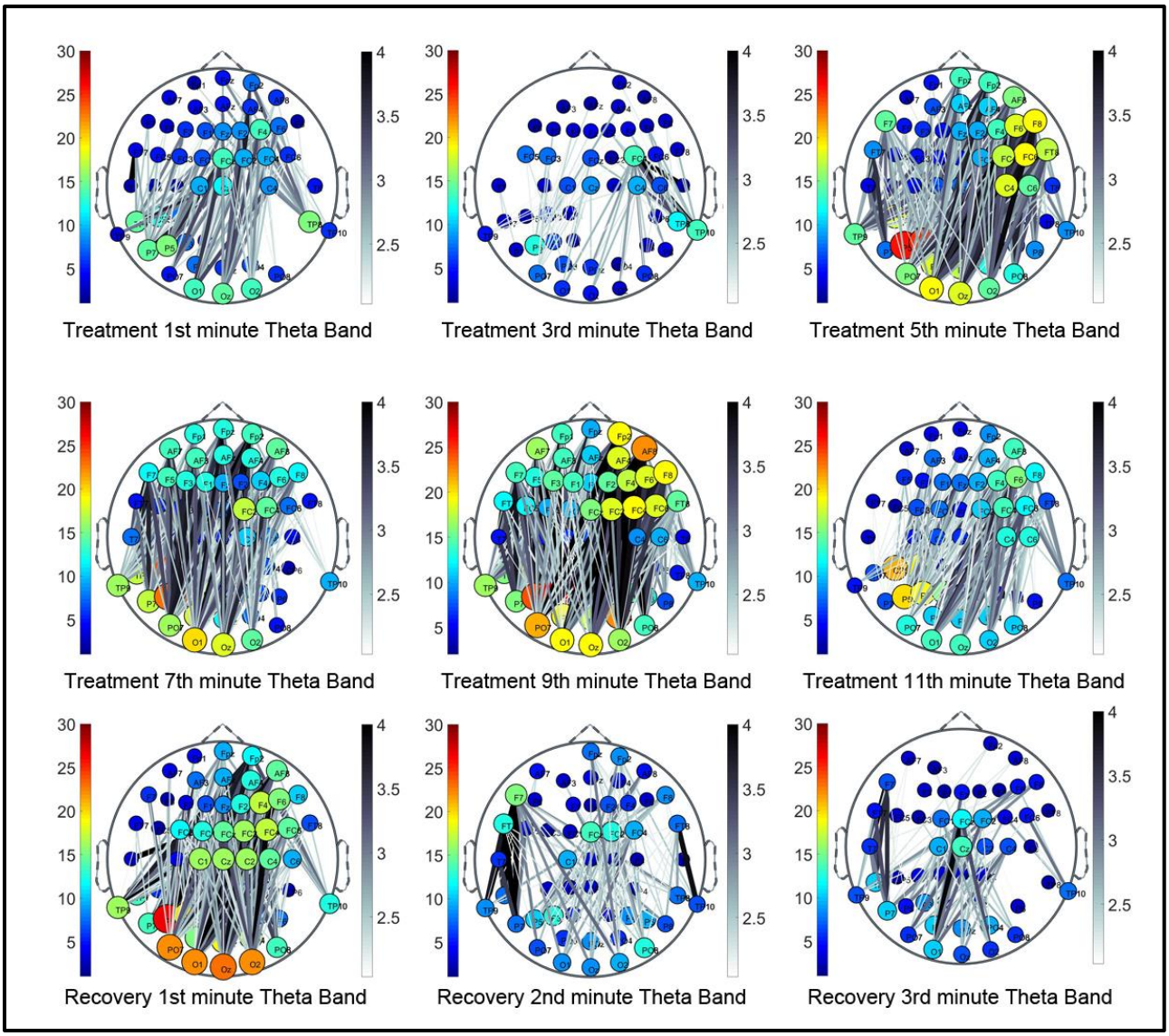

(b)

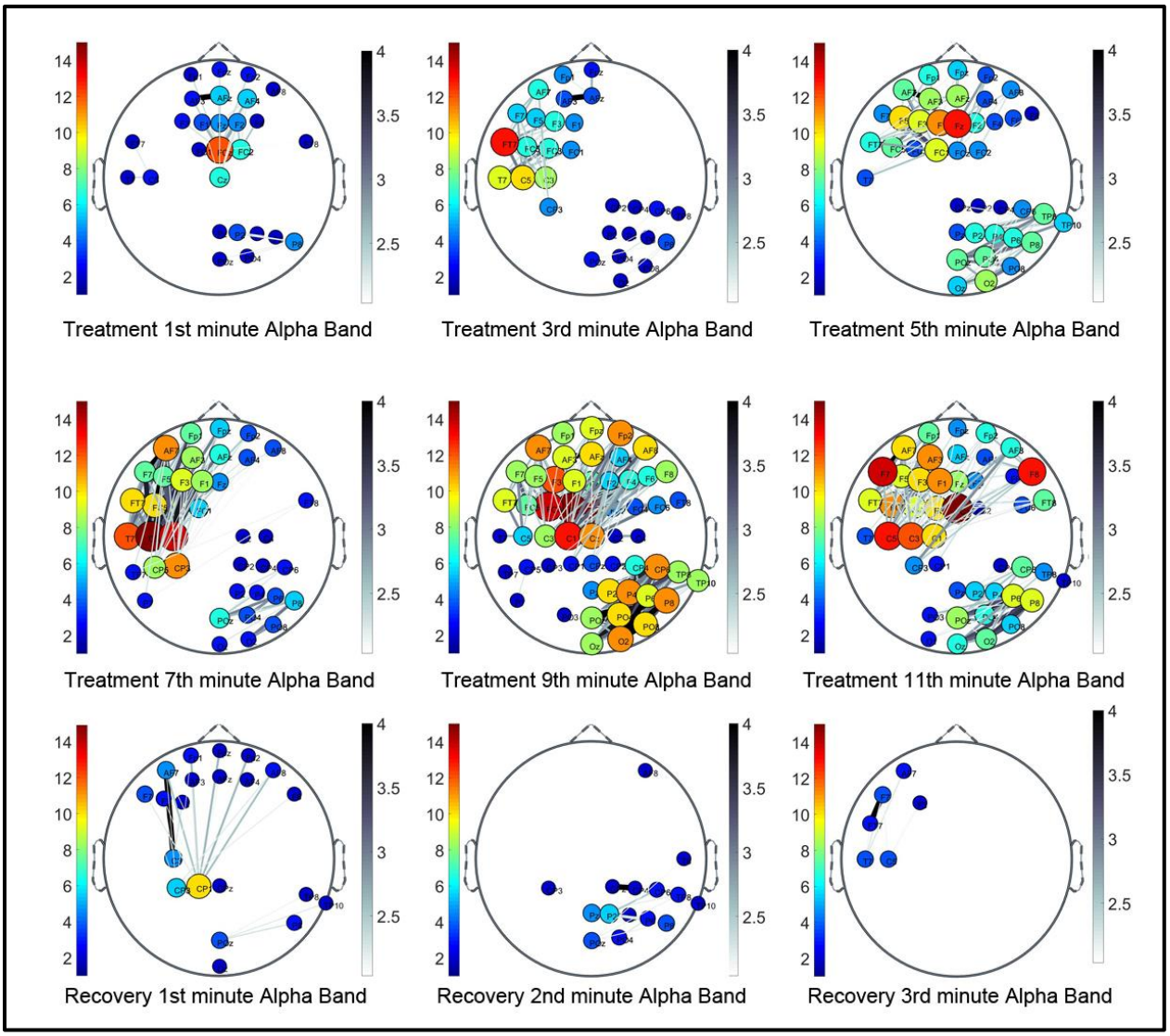

Figure 3.4: Significant connections between different regions on the scalp. Two different bands are represented: (a) theta band and (b) alpha band. In each subplot, grey color bar on the right side represents the T value, which also reflects the strength of connection between two nodes. The color bar on the left side represents the number of connections at each node, which indicates the strength of connection at specific nodes.

From figure 3.4(a), it can be observed that the right frontal region had relativly more number of significant connections as compared to the left frontal region in the theta band. This is illustrated by the size and color of the nodes in that region. However, occipital region did not follow the same trend. The left occipital region had more number of significant connections as

compared to the right occipital region. Furthermore, dense connections were formed between the right frontal region and left occipital region of the brain in the theta band. This phenomenon was clearly demonstrated from the 5th minute until 11th minute of laser treatment. However, as soon as the recovery phase began, the overall significant connections were reduced.

The results from the alpha band were in contrast with the theta band, as depicted in fig 3.4(b). It can be observed that in alpha band the left frontal region had relativly more number of significant connections as compared to the right frontal region. This is illustrated by the size and color of the nodes in that region. However, occipital region did not follow the same trend for alpha band as well. The right occipital region had more number of significant connections as compared to the left occipital region. Dense connections were formed between the left frontal region and right occipital region of the brain in the alpha band. This phenomenon was clearly demonstrated from the 5th minute uptil 11th minute during laser treatment. However, as soon as the recovery phase began, the overall significant connections were also much reduced.

I also wanted to observe percentage of significant connections (PSC) in each time segment of alpha band and theta band. Total number of connections of one electrode with other 63 electrodes was 1 x 63 = 63. So, there were 63 possible connections of one electrode to the other electrodes. To calculate the total number of connections for 64 electrodes system, I would have 64 x 63 = 4032, so there were total a number of 4032 possible connections.

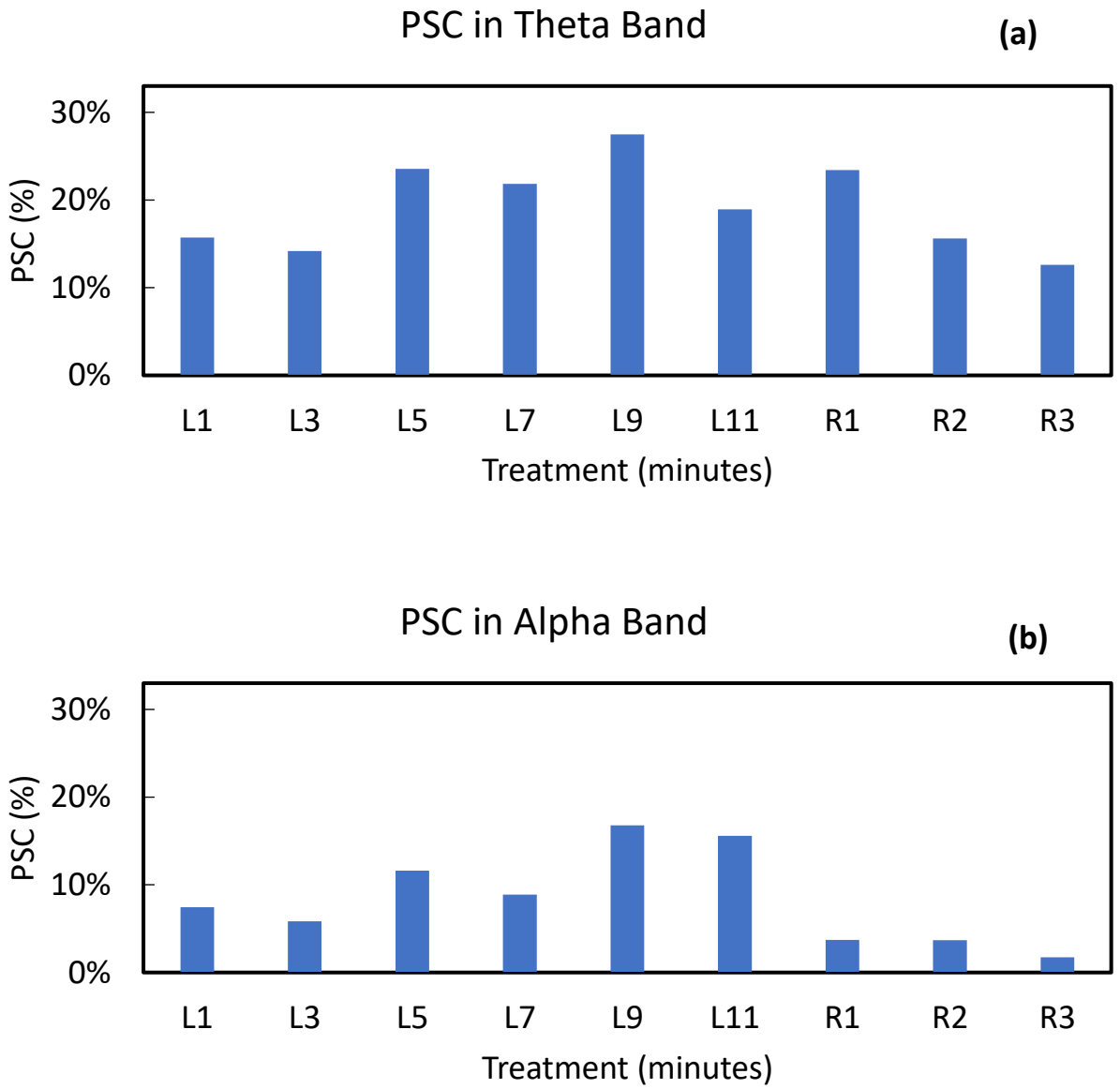

Figure 3.5: Percentage of significant connection for each treatment duration in: (a) Theta Band and (b) Alpha band. The x-axis represents time duration of treatment, which is in minutes; y-axis represents Percentage of Significant Connections (PSC). Each bar is representing the percentage of significant connections out of total number of connections per minute.

In figure 3.5, it has been observed that during laser treatment both theta and alpha band were significantly affected. A gradual increase in the number of significant connections were noticed until the recovery phase. Theta band and alpha band had the most significant number

of connections in the 9th minute of treatment, resulting in the maximum brain network change administered by the laser dose. After the treatment ends, number of significant connections were reduced, illustrated by downward trend in the recovery phase. From figure 3.5, overall trend is consistent for the theta band and alpha band.

3.4 Discussion:

From this study my aim was to investigate the changes in the brain network caused by TPBM in the lower freqeuncy bands. To the best of my knowledge, this is one of the first studies observing the changes in electrophysiological signals of the brain network with the application of 1064-nm laser.

3.4.1 Potential improvement in memory by TPBM

Low oscillations synchronization has been extensively studied in different aspects of memory, which are: memory speed effect, frequency rhythm, and memory processes. These aspects can be explained in terms of brain oscillations [48]. Low oscillation signals are associated with high synaptic strength that makes the memory retrieval very easy [49]. Moreover, memory-related oscillations are confined to alpha and theta bands [48, 50]. Particularly, theta activity is high during the encoding phase of the memory and plays a vital role in episodic long term memory [51, 52]. In numerous studies, theta band is found to have high oscillation activity in different memory retention tasks [53, 54]. From the litreature review, it has been observed that activity of low frequency bands are very important for different aspects of the memory; that are retention, encoding and retreival.

The frontal part of the brain is responsible for multiple cognitive and executive functions, such as decision making, working memory, and cognitive tasks [53], whereas the posterior and parietal areas are responsible for short term memory [53]. Increase of memory retention leads to an increase in the activity of theta synchronization in the temporal and frontal region [55, 56]. From this study, it has been observed that significant connections are formed between the frontal/anterior and parietal/posterior region of the brain by the administration of TPBM. Thus, I have **Speculation 1:** The adminsitration of TPBM on the right forehead enhances the cognitive functions and learning activity.

3.4.2 Modulation of neuronal activity by TPBM

The increase in the tissue oxygenation and ATP synthesis takes place due to photo-biomodulation, by the upregulation of CCO [37, 43], as reported by our group. Specifically, the first study reported the upregulation of oxidized CCO and increase in hemoglobin concentration of the human forearm by the stimulation using 1064nm laser [37]. The second study reported the upregulation of oxidized [CCO] and increases of [HbO] and [HbT] in the human brain, also induced by the 1064 nm laser [43].

Based on those two studies, I have **Speculation 2**: Neurons can be activated by the energy provided from the ATP synthesis, which will promote or release neurotransmitters for conducting or propagating electrophysiological signals through theta and alpha frequencies. Subsequently, Information will be exchanged or passed effectively with different parts of the brain in low frequency oscillations.

3.4.3 Validation for treating neurodegenerative diseases by TPBM

Multiple studies have shown that TPBM produces cognition or memory improvements in patients with different nuerodegenrative diseases [16, 23]. Other studies have also demonstrated thatcertain brain diseases decrease the alpha waves [48, 57, 58]. From my research, it is observed increases in the activity of alpha band during the laser treatmentas shown in fig 3.4. So, I have **Speculation 3**: Both alpha and theta waves are enhanced by TPBM, which could potentially be the mechanistic reason for improving different brain disorders by TPBM. However, this speculation needs much validation in future studies.

3.4.4 Interaction between different oscillation bands by TPBM

Low frequency bands, particularly theta band, interact with other frequency bands for cognitive functions. It is extensively found in literature that theta oscillations are involved in interaction with higher frequency oscillations for improving memory performance [55, 59]. During a working memory task, there is a synchronization between frontal midline theta and gamma oscillations [51]. Furthermore, working memory retention has a strong theta synchronization between frontal region and parietal region [60, 61]. TPBM is increasing the number of connections in lower frequency band, as observed in fig 3.5. But, in my study, I did not perform any analysis in this direction, which can carried out in future studies.

3.5 Limitation of the study

I used the Pearson correlation analysis in this study to calculate functional connectivity. [27, 44-47]. I could have used more robust EEG analysis tehniques to overcome volume conduction problem by utilizing the phase locking value (PLV) or phase lag index (PLI) methods which can also lead to quantifications of casual relations and directionality of information flow

among different scalp locations. In addition, in this study, I analyzed the functional connectivity over 20 subjects. To make results more reliable, more subjects could be studied.

3.6 Conclusion

My aim in this Chapter was to investigate the functional connectivity of the human brain network under TPBM using 64-channel EEG. The results showed that TPBM improved a significant number of connections in two lower oscialltion bands across the human brain. Such enhancement of brain network by 1064-nm laser stimulation may be associated with the underlying principle/mechanism on why TPBM can improve human cognition and memory functions.

CHAPTER 4

SUMMARY AND FUTURE WORK

4.1 Summary

Previously, very few experiments have been performed to quantify light fluence within the human tissue or tissue phantoms from a large-sized laser source (having diameters of 2, 3, or 4 cm) at different wavelengths. My primary aim was to address this issue by perfoming different experiments in the tissue phantom. These experiments included the estimation of optical fluence as a function of: laser power or irradiance, area of beam size, and penetration depth.

The experiments were performed and described in details in Chapter 2, and the results were analyzed and reported thoroughly also in Chapter 2. From this first set of experiment, it was observed that the laser fluence at a given depth with a fixed aperture size had a linear relationship with the optical irradiance or laser power. Two separate studies were performed for the comparision with the analytical solution with different beam size areas and at different penetration depths. In both cases, the results showed simliar or consistent trends between the experimental results and analytical solution. Furthermore, the absorption coefficient of the tissue phantom solution at 1064 nm can be estimated using the analytical solution.

My second aim targeted the investigation of electrophysiological study of the brain EEG signals altered under TPBM. From this study, it was observed that TPBM is able to modulate the brain signals at lower frequency bands, i.e., theta and alph bands. There was a gradual increase in the number of significant connections in lower oscialltion bands as the laser was administered before the recovery period. In principle, slower oscialltions are generally involved in many

cognitive functions, and therefore the increase of significant connections in those bands may potentially be explained as a result of TPBM.

4.2 Future Work

4.2.1 Future work for Aim 1

The importance of this study lies in the investigation of optical fluence of 1064-nm laser within biological tissue for the effective treatment of different neurological disorders. According to literature, several studies on animal models have utilized wavelength light sources in the range of 810 nm to 840 nm [16]. For future studies, it is necessary to investigate and compare the optical fleunce of 810-nm laser and 850-nm LED with that of the 1064-nm laser, under similar conditions. This compairison will help identify the optimized wavelength for TPBM to be used in future for treating different neurological disorders.

4.2.2 Future work for Aim 2

The approach of combining PBM with electrophysiology has a lot of potential for further research in neuroscience. There are only a few studies carried out on TPBM with the application of electrophysiology. For aim 2, I studied the functional connectivity in the human brain at lower frequency bands during the TPBM using 1064nm laser.

In future, I suggest to add more parameters to the current experimental protocol in order to observe and compare changes in the brain network. A few other interests for future studies will be:

1. To investigate effects of laser power densities on the brain network by measuring scalp electrophysiological signals from the human brain utilizing the 1064-nm laser.

2. To administer the laser dose on the left forehead and compare the results with the current study.

For data analysis, I suggest to normalize the data from baseline before calculating the functional connectivity. Moreover, EEG data can be analyzed by graph theory method for calculating different network parameters, including small world, efficiency, rich club, and assortavity [62]. Also, the information flow estimation and modelling causal relationship between different brain regions using a multivariate model [63] can be other possible alternatives.

References

1. Yu, J.-M., et al., *Phantom verification for a ring-scanning and prone diffuse optical imaging system.* Optics Communications, 2017. **405**: p. 177-184.
2. Cerussi, A.E., et al., *Sources of absorption and scattering contrast for near-infrared optical mammography.* Acad Radiol, 2001. **8**(3): p. 211-8.
3. Salo, D., et al., *Multispectral measurement of contrast in tissue-mimicking phantoms in near-infrared spectral range of 650 to 1600 nm.* Journal of Biomedical Optics, 2014. **19**(8): p. 086008.
4. Sandell, J.L. and T.C. Zhu, *A review of in-vivo optical properties of human tissues and its impact on PDT.* Journal of Biophotonics, 2011. **4**(11-12): p. 773-787.
5. Schroeder, P., et al., *Photoprotection beyond ultraviolet radiation--effective sun protection has to include protection against infrared A radiation-induced skin damage.* Skin Pharmacol Physiol, 2010. **23**(1): p. 15-7.
6. Wong-Riley, M.T., et al., *Photobiomodulation directly benefits primary neurons functionally inactivated by toxins: role of cytochrome c oxidase.* J Biol Chem, 2005. **280**(6): p. 4761-71.
7. Conlan, M.J., J.W. Rapley, and C.M. Cobb, *Biostimulation of wound healing by low-energy laser irradiation. A review.* J Clin Periodontol, 1996. **23**(5): p. 492-6.
8. Whelan, H.T., et al., *Effect of NASA light-emitting diode irradiation on wound healing.* J Clin Laser Med Surg, 2001. **19**(6): p. 305-14.
9. Avci, P., et al., *Low-level laser (light) therapy (LLLT) in skin: stimulating, healing, restoring.* Seminars in cutaneous medicine and surgery, 2013. **32**(1): p. 41-52.
10. Yu, W., et al., *Photomodulation of oxidative metabolism and electron chain enzymes in rat liver mitochondria.* Photochem Photobiol, 1997. **66**(6): p. 866-71.
11. Mester, E., B. Szende, and P. Gartner, *[The effect of laser beams on the growth of hair in mice].* Radiobiol Radiother (Berl), 1968. **9**(5): p. 621-6.
12. Hashmi, J.T., et al., *Role of Low-Level Laser Therapy in Neurorehabilitation.* PM & R : the journal of injury, function, and rehabilitation, 2010. **2**(12 Suppl 2): p. S292-S305.
13. Madison, H. and R.H. Michael, *Photobiomodulation and the brain: a new paradigm.* Journal of Optics, 2017. **19**(1): p. 013003.
14. Tuby, H., L. Maltz, and U. Oron, *Low-level laser irradiation (LLLI) promotes proliferation of mesenchymal and cardiac stem cells in culture.* Lasers Surg Med, 2007. **39**(4): p. 373-8.
15. Oron, U., et al., *Enhanced liver regeneration following acute hepatectomy by low-level laser therapy.* Photomed Laser Surg, 2010. **28**(5): p. 675-8.
16. Hennessy, M. and M.R. Hamblin, *Photobiomodulation and the brain: a new paradigm.* Journal of optics (2010), 2017. **19**(1): p. 013003.
17. Michalikova, S., et al., *Emotional responses and memory performance of middle-aged CD1 mice in a 3D maze: effects of low infrared light.* Neurobiol Learn Mem, 2008. **89**(4): p. 480-8.
18. Rojas, J.C., et al., *Neuroprotective effects of near-infrared light in an in vivo model of mitochondrial optic neuropathy.* The Journal of neuroscience : the official journal of the Society for Neuroscience, 2008. **28**(50): p. 13511-13521.
19. Lapchak, P.A., et al., *Transcranial Near-Infrared Laser Transmission (NILT) Profiles (800 nm): Systematic Comparison in Four Common Research Species.* PLoS ONE, 2015. **10**(6): p. e0127580.
20. Salehpour, F. and S.H. Rasta, *The potential of transcranial photobiomodulation therapy for treatment of major depressive disorder.* Rev Neurosci, 2017. **28**(4): p. 441-453.
21. Schiffer, F., et al., *Psychological benefits 2 and 4 weeks after a single treatment with near infrared light to the forehead: a pilot study of 10 patients with major depression and anxiety.* Behavioral and Brain Functions : BBF, 2009. **5**: p. 46-46.

22. Naeser, M.A., et al., *Acupuncture in the treatment of paralysis in chronic and acute stroke patients--improvement correlated with specific CT scan lesion sites.* Acupunct Electrother Res, 1994. **19**(4): p. 227-49.
23. Maksimovich, I.V., *Dementia and Cognitive Impairment Reduction after Laser Transcatheter Treatment of Alzheimer¡¯s Disease.* World Journal of Neuroscience, 2015. **Vol.05No.03**: p. 15.
24. Cassano, P., et al., *Review of transcranial photobiomodulation for major depressive disorder: targeting brain metabolism, inflammation, oxidative stress, and neurogenesis.* Neurophotonics, 2016. **3**(3): p. 031404.
25. Huang, Y.-Y., et al., *Transcranial low level laser (light) therapy for traumatic brain injury.* Journal of biophotonics, 2012. **5**(11-12): p. 827-837.
26. Jurcak, V., D. Tsuzuki, and I. Dan, *10/20, 10/10, and 10/5 systems revisited: Their validity as relative head-surface-based positioning systems.* NeuroImage, 2007. **34**(4): p. 1600-1611.
27. van Mierlo, P., et al., *Functional brain connectivity from EEG in epilepsy: seizure prediction and epileptogenic focus localization.* Prog Neurobiol, 2014. **121**: p. 19-35.
28. Elson, J.M. and J.M. Bennett, *Calculation of the power spectral density from surface profile data.* Applied Optics, 1995. **34**(1): p. 201-208.
29. Hamblin, M.R., *Shining light on the head: Photobiomodulation for brain disorders.* BBA Clinical, 2016. **6**: p. 113-124.
30. Kolb, B. and I.Q. Whishaw, *Brain plasticity and behavior.* Annu Rev Psychol, 1998. **49**: p. 43-64.
31. Tedford, C.E., et al., *Quantitative analysis of transcranial and intraparenchymal light penetration in human cadaver brain tissue.* Lasers Surg Med, 2015. **47**(4): p. 312-22.
32. Jagdeo, J.R., et al., *Transcranial red and near infrared light transmission in a cadaveric model.* PLoS One, 2012. **7**(10): p. e47460.
33. Pitzschke, A., et al., *Red and NIR light dosimetry in the human deep brain.* Phys Med Biol, 2015. **60**(7): p. 2921-37.
34. Yaroslavsky, A.N., et al., *Optical properties of selected native and coagulated human brain tissues in vitro in the visible and near infrared spectral range.* Phys Med Biol, 2002. **47**(12): p. 2059-73.
35. Henderson, T.A. and L.D. Morries, *Near-infrared photonic energy penetration: can infrared phototherapy effectively reach the human brain?* Neuropsychiatr Dis Treat, 2015. **11**: p. 2191-208.
36. Blanco, N.J., W.T. Maddox, and F. Gonzalez-Lima, *Improving executive function using transcranial infrared laser stimulation.* Journal of neuropsychology, 2017. **11**(1): p. 14-25.
37. Wang, X., et al., *Interplay between up-regulation of cytochrome-c-oxidase and hemoglobin oxygenation induced by near-infrared laser.* Scientific Reports, 2016. **6**: p. 30540.
38. Tian, F., et al., *Transcranial laser stimulation improves human cerebral oxygenation.* Lasers in Surgery and Medicine, 2016. **48**(4): p. 343-349.
39. dos Santos, S.A., et al., *Effects of Photobiomodulation Therapy on Oxidative Stress in Muscle Injury Animal Models: A Systematic Review.* Oxidative Medicine and Cellular Longevity, 2017. **2017**: p. 5273403.
40. Rizzi, C.F., et al., *Effects of low-level laser therapy (LLLT) on the nuclear factor (NF)-kappaB signaling pathway in traumatized muscle.* Lasers Surg Med, 2006. **38**(7): p. 704-13.
41. Ribeiro, B.G., et al., *Red and Infrared Low-Level Laser Therapy Prior to Injury with or without Administration after Injury Modulate Oxidative Stress during the Muscle Repair Process.* PLoS One, 2016. **11**(4): p. e0153618.
42. Davila, S., et al., *Low level laser therapy on experimental myopathy.* Laser Ther, 2011. **20**(4): p. 287-92.

43. Wang, X., et al., *Up-regulation of cerebral cytochrome-c-oxidase and hemodynamics by transcranial infrared laser stimulation: A broadband near-infrared spectroscopy study.* J Cereb Blood Flow Metab, 2017. **37**(12): p. 3789-3802.
44. van Diessen, E., et al., *Opportunities and methodological challenges in EEG and MEG resting state functional brain network research.* Clin Neurophysiol, 2015. **126**(8): p. 1468-81.
45. Wendling, F., et al., *From EEG signals to brain connectivity: a model-based evaluation of interdependence measures.* J Neurosci Methods, 2009. **183**(1): p. 9-18.
46. Ma, X., et al., *Brain Connectivity Variation Topography Associated with Working Memory.* PLOS ONE, 2016. **11**(12): p. e0165168.
47. Clemens, B., et al., *Increased resting-state EEG functional connectivity in benign childhood epilepsy with centro-temporal spikes.* Seizure, 2016. **35**: p. 50-5.
48. Klimesch, W., *Memory processes, brain oscillations and EEG synchronization.* International Journal of Psychophysiology, 1996. **24**(1): p. 61-100.
49. Heib, D.P.J., et al., *Slow Oscillation Amplitudes and Up-State Lengths Relate to Memory Improvement.* PLOS ONE, 2013. **8**(12): p. e82049.
50. Klimesch, W., et al., *A short review of slow phase synchronization and memory: evidence for control processes in different memory systems?* Brain Res, 2008. **1235**: p. 31-44.
51. Griesmayr, B., et al., *Human frontal midline theta and its synchronization to gamma during a verbal delayed match to sample task.* Neurobiology of Learning and Memory, 2010. **93**(2): p. 208-215.
52. Osipova, D., et al., *Theta and Gamma Oscillations Predict Encoding and Retrieval of Declarative Memory.* The Journal of Neuroscience, 2006. **26**(28): p. 7523-7531.
53. Baddeley, A., *The episodic buffer: a new component of working memory?* Trends Cogn Sci, 2000. **4**(11): p. 417-423.
54. Jensen, O. and C.D. Tesche, *Frontal theta activity in humans increases with memory load in a working memory task.* Eur J Neurosci, 2002. **15**(8): p. 1395-9.
55. Sauseng, P., et al., *Control mechanisms in working memory: a possible function of EEG theta oscillations.* Neurosci Biobehav Rev, 2010. **34**(7): p. 1015-22.
56. Womelsdorf, T., et al., *Theta-activity in anterior cingulate cortex predicts task rules and their adjustments following errors.* Proceedings of the National Academy of Sciences, 2010. **107**(11): p. 5248-5253.
57. Klimesch, W., *EEG-alpha rhythms and memory processes.* Int J Psychophysiol, 1997. **26**(1-3): p. 319-40.
58. Vlahou, E.L., et al., *Resting-state slow wave power, healthy aging and cognitive performance.* Scientific Reports, 2014. **4**: p. 5101.
59. Nyhus, E. and T. Curran, *Functional role of gamma and theta oscillations in episodic memory.* Neurosci Biobehav Rev, 2010. **34**(7): p. 1023-35.
60. Mizuhara, H. and Y. Yamaguchi, *Human cortical circuits for central executive function emerge by theta phase synchronization.* Neuroimage, 2007. **36**(1): p. 232-44.
61. Sarnthein, J., et al., *Synchronization between prefrontal and posterior association cortex during human working memory.* Proceedings of the National Academy of Sciences of the United States of America, 1998. **95**(12): p. 7092-7096.
62. Bullmore, E. and O. Sporns, *Complex brain networks: graph theoretical analysis of structural and functional systems.* Nat Rev Neurosci, 2009. **10**(3): p. 186-98.
63. van Mierlo, P., et al., *Functional brain connectivity from EEG in epilepsy: Seizure prediction and epileptogenic focus localization.* Progress in Neurobiology, 2014. **121**: p. 19-35.